OPEN BIOLOGY

Methods and techniques

Authors for correspondence:
Tõnis Laasfeld
e-mail: laasfeld@ut.ee
Ago Rinken
e-mail: ago.rinken@ut.ee

†These authors contributed equally to this study.

THE ROYAL SOCIETY PUBLISHING

Live-cell microscopy or fluorescence anisotropy with budded baculoviruses— which way to go with measuring ligand binding to M4 muscarinic receptors?

Maris-Johanna Tahk[1,†], Jane Torp[1,†], Mohammed A. S. Ali[2], Dmytro Fishman[2], Leopold Parts[2,3], Lukas Grätz[4], Christoph Müller[4], Max Keller[4], Santa Veiksina[1], Tõnis Laasfeld[1,2] and Ago Rinken[1]

[1]Institute of Chemistry, University of Tartu, Ravila 14a, 50411 Tartu, Estonia
[2]Department of Computer Science, University of Tartu, Narva Street 20, 51009 Tartu, Estonia
[3]Wellcome Sanger Institute, Wellcome Genome Campus, Hinxton, Cambridgeshire, UK
[4]Institute of Pharmacy, Faculty of Chemistry and Pharmacy, University of Regensburg, Universitätsstrasse 31, 93053 Regensburg, Germany

M-JT, 0000-0002-4566-9192; JT, 0000-0003-3257-8483; MASA, 0000-0002-0266-4703; DF, 0000-0002-4644-8893; LP, 0000-0002-2618-670X; LG, 0000-0001-6755-0742; CM, 0000-0001-6121-6292; MK, 0000-0002-8095-8627; SV, 0000-0003-4191-4354; TL, 0000-0002-4730-3047; AR, 0000-0002-7238-749X

M4 muscarinic acetylcholine receptor is a G protein-coupled receptor (GPCR) that has been associated with alcohol and cocaine abuse, Alzheimer's disease, and schizophrenia which makes it an interesting drug target. For many GPCRs, the high-affinity fluorescence ligands have expanded the options for high-throughput screening of drug candidates and serve as useful tools in fundamental receptor research. Here, we explored two TAMRA-labelled fluorescence ligands, UR-MK342 and UR-CG072, for development of assays for studying ligand-binding properties to M4 receptor. Using budded baculovirus particles as M4 receptor preparation and fluorescence anisotropy method, we measured the affinities and binding kinetics of both fluorescence ligands. Using the fluorescence ligands as reporter probes, the binding affinities of unlabelled ligands could be determined. Based on these results, we took a step towards a more natural system and developed a method using live CHO-K1-hM4R cells and automated fluorescence microscopy suitable for the routine determination of unlabelled ligand affinities. For quantitative image analysis, we developed random forest and deep learning-based pipelines for cell segmentation. The pipelines were integrated into the user-friendly open-source Aparecium software. Both image analysis methods were suitable for measuring fluorescence ligand saturation binding and kinetics as well as for screening binding affinities of unlabelled ligands.

1. Introduction

Muscarinic acetylcholine receptors (mAChR) are a group of G protein-coupled receptors (GPCRs) with five subtypes M1–M5 which play a crucial role in, for example, the regulation of memory, heart and bladder function, and dopaminergic neurotransmission [1–4]. Lately, the M4R has been suggested to be a potential drug target for the treatment of neurodegenerative and neuropsychiatric disorders like Alzheimer's disease or schizophrenia [5,6]. Furthermore, as new links emerge between the M4 receptor and alcoholism, as well as between M4 receptor polymorphism and cocaine and heroin abuse, the M4 receptor becomes an even more versatile drug target [7,8]. Despite the growing importance, the

development of novel drugs targeting the M_4 receptor is difficult as the similarity of orthosteric binding sites of all mAChR leads to low subtype selectivity of ligands [9]. One solution is the development of allosteric modulators, which may exhibit higher subtype selectivity but relatively lower affinities [10]. To find suitable drugs, ligand screening remains an important step in the drug development process. Screening for new drug candidates using fluorescence methods has become quite popular due to several advantages over radioligand-based assays [11]. However, until now, only a limited number of fluorescence ligands have been available for mAChR, and to our knowledge, none have been extensively used to develop assays to study M_4 receptors [12–14]. Recently, several novel low molecular weight fluorescently labelled ligands targeting mAChRs were described [15,16]. Of these ligands, TAMRA labelled UR-CG072 and UR-MK342 have already been successfully used for studying M_2 receptors in NanoLuc luciferase bioluminescence resonance energy transfer (nanoBRET) and fluorescence anisotropy (FA) assays [17]. Even though these ligands show a slight preference for the M_2 receptor, they still have a high affinity for M_1 and M_4 receptors. Therefore, the new fluorescent ligands should be suitable as probes for studying M_4 receptors in drug candidate screening assays as well as in a large variety of fluorescence microscopy techniques from live tissue systems to single-molecule studies [18–20].

One of the most common options for characterizing fluorescent probe binding to proteins, including GPCRs, is the FA method [21–25]. For the successful development of FA assays, several unique aspects must be considered. Most importantly, FA is a ratiometric assay with its value depending on the ratio of bound and free ligand. Therefore, all experiments must be designed in a way that the probe and receptor concentrations are in a similar range, which means that ligand and receptor depletion should be taken into account [26]. The main advantage of the FA method is that there is no need to separate bound ligand from the free ligand, making it easy to continuously collect time-course data during ligand binding. These time-course data can be used to obtain kinetic parameters and to develop reaction kinetics models of ligand binding for more insight into the complicated regulation of signal transduction. In addition to cell membranes, budded baculovirus (BBV) particles can serve as a high-quality receptor source for FA assays. BBV particles are advantageous because they have a fixed cylindrical shape (approx. 50 nm × 300 nm) and homogeneous size distribution, resulting in minimal noise and small variability between replicates compared to membrane preparations [26–28]. Due to the small size and low sedimentation rate of BBV particles, they are well suited for performing homogeneous assays. However, downstream signalling cascades are not present in BBV particles. Furthermore, BBV particles are produced in Sf9 insect cells, where the membrane composition differs from mammalian systems.

Most of these problems can be avoided by using more natural live-cell assays for receptor display. Among multiple developed assays [29], NanoBRET has gained a lot of popularity in recent years due to its homogeneous format, the possibility of real-time measurements and relatively good compatibility with a wide array of fluorophores. However, it requires genetically modified receptors, which may have an influence on ligand binding and receptor activation [30]. Studying wild-type receptors is more difficult, as the receptor cannot be tagged, which in turn does not allow to take advantage of the high sensitivity of bioluminescence approaches. Further, the plate reader-based

RET methods only provide cell population average statistics instead of single-cell resolution information, which may hide some important effects. One solution to both problems is flow cytometry, which can measure fluorescent ligand binding to individual cells. However, it cannot follow binding to a single cell over time nor spatially resolve from which part of the cell the fluorescence originates from [31]. By contrast, high-throughput microscopy can provide spatial information as well as time-course information for the same cells, making more detailed analysis possible. On the downside, extracting pharmacologically relevant quantitative information from the bioimages requires more complex data analysis algorithms. However, once an automated data analysis solution with user-friendly software exists, it can be reused in future studies.

Microscopy methods open many possibilities for assay setup, but performing time-resolved measurements with the cellular resolution is not trivial and existing methods have several potential issues [32]. In previously published works, the kinetics of ligand binding to live cells in an high-throughput screening (HTS) compatible manner have only been analysed by the fluorescence intensity of the whole image [33,34]. For these methods, it is necessary to seed cells consistently as a high confluency monolayer, but this is either difficult or practically impossible to achieve with some cell lines [35]. Furthermore, it is much more difficult to identify individual cells from a dense monolayer, thus reducing the number of parameters that can be studied. In addition, dense monolayers can significantly affect physico-chemical environmental parameters such as oxygen concentration which can also have more direct effects on muscarinic receptor signalling [36]. For example, transient hypoxic conditions lead to increased phosphorylation of M_1 and M_2 receptors [37]. Finally, dense cell monolayers can easily cause focusing errors in automated microscopy, as some cells may have detached or formed a second layer.

A better approach was developed with HEK-293-D_3R cells, which uses a machine-learning algorithm for detecting only the fluorescence intensity originating from cell membranes in equilibrium conditions and does not rely on dense monolayers [35]. However, ligand-binding kinetics were not analysed in that study. Nevertheless, kinetic measurements should be possible with a similar setup after adjusting the experimental design and the image analysis pipeline.

The most difficult steps of microscopy image analysis are usually cell detection and segmentation, which is necessary for robust quantification of the fluorescence signal. Approaches for these tasks have gone through a paradigm shift from classical computer vision techniques to machine learning and especially deep-learning (DL) methods. Deep neural networks dominate most of the developed benchmark datasets for general problems as well as bioimage analysis specifically [38–40]. A large number of DL architectures have been developed over the past few years, but their wide application can be limited by compatibility issues with popular image analysis software and too complex design for comprehensive understanding for life scientists [41–48]. Therefore, a widely supported and well-known U-Net architecture is used in the present study for cell segmentation from bright-field images, as it has shown good results for similar microscopy images [43,49].

In this study, we developed new fluorescence-based ligand-binding assays for the M_4 receptor. These assays use two recently developed 5-carboxytetramethylrhodamine (5-TAMRA) labelled dibenzodiazepinone derivatives, UR-MK342 and

UR-CG072 [16], and two different receptor sources. As both BBV particle-based FA and live cell-based microscopy assays have distinct advantages, we studied and compared the two options and discovered that both options are viable. To our best knowledge, this is the first detailed description of M_4 receptor fluorescence ligand-binding assays, which opens up many new possibilities to study these receptors.

2. Material and methods

2.1. Materials

Assay buffer consisted of MilliQ water, 135 mM NaCl (Appli-Chem, Darmstadt, Germany), 1 mM $CaCl_2$ (AppliChem), 5 mM KCl (AppliChem), 1 mM $MgCl_2$ (AppliChem), 11 mM Na-HEPES (pH = 7.4) (Sigma-Aldrich, Taufkirchen, Germany), protease inhibitor cocktail (according to the manufacturer's description, Roche, Basel, Switzerland) and 0.1% Pluronic F-127 (Sigma-Aldrich).

Muscarinic acetylcholine receptor ligands acetylcholine, arecoline, pirenzepine, pilocarpine, atropine and scopolamine were purchased from Sigma-Aldrich and carbachol from Tocris Bioscience (Abingdon, UK). The syntheses of the fluorescent ligands UR-MK342 and UR-CG072 [16] and the dualsteric M_2R ligands UR-SK59 [50], UR-SK75 [50] and UNSW-MK259 [51], showing also high M_4R affinity, were described previously. All ligand stock solutions were prepared using cell culture grade DMSO (AppliChem) and stored at −20°C.

2.2. Cell culture

Spodoptera frugiperda Sf9 (Invitrogen Life Technologies, Schwerte, Germany) cells were maintained as a suspension culture in serum-free insect cell growth medium EX-CELL 420 (Sigma-Aldrich) at 27°C in a non-humidified environment.

Non-transfected Chinese hamster ovary cells (CHO-K1) were purchased from ATCC, LGC Standards (Wesel, Germany), and CHO-K1 expressing human M_4 receptor (CHO-K1-hM$_4$R cells) were obtained from Missouri S&T cDNA Resource Centre (Bloomsberg, USA). The M_4 receptor expression level has been previously determined to be 1×10^5 and 4×10^5 [^{3}H]NMS binding sites per cell [51]. CHO-K1 cells were cultured in Dulbecco's Modified Eagle Medium/ Nutrient Mixture F-12 (DMEM/F12) (Sigma-Aldrich) with 9% FBS (Sigma-Aldrich), antibiotic antimycotic solution (100 U ml^{-1} penicillin, 0.1 mg ml^{-1} streptomycin, 0.25 μg ml^{-1} amphotericin B) (Sigma-Aldrich) and for CHO-K1-hM$_4$R 750 μg ml^{-1} of selection antibiotic geneticin (G418) (Capricorn Scientific, Ebsdorfergrund, Germany) were added. All mammalian cells were grown in a humidified incubator at 37°C with 5% CO_2 until 90% confluency. To detach the cells from the plate, 0.05% trypsin with EDTA (Gibco, Paisley, Scotland) was used.

Cell culture viability and density were determined with an Automated Cell Counter TC20 (Bio-Rad Laboratories, Sundyberg, Sweden) by the addition of 0.2% trypan blue (Sigma-Aldrich). All experiments with CHO-K1-hM$_4$R, CHO-K1 and Sf9 cell cultures were performed with passages 40–50, 33 and 2–25, respectively. Mammalian cell lines were tested and determined to be mycoplasma-negative.

2.3. Preparation of budded baculovirus particles

The human M_4 receptor in pcDNA3.1+ was purchased from cDNA Resource Center (www.cdna.org), and manufacturing and production of BBV containing human M_4 receptor were performed as described in [25] with some modification. For cloning M_4 into pFastBac vector, BamHI and XbaI sites were used with enzymes from (Thermo Fisher Scientific, Schwerte, Germany). To transform the bacmid into Sf9 cells, the transfection reagent FuGene 6 (Promega Corporation, Madison, USA) was used according to the manufacturer's protocol. After the viruses were generated and collected, the amount of infectious viral particles per ml (IVP/ml) for all the baculoviruses was determined with the image-based cell size estimation assay [52].

To produce the BBV particles, Sf9 cells were infected with multiplicity of infection (MOI) = 3 and incubated for 4 days (end viability of Sf9 cells was 55%). The supernatant, containing BBV particles, was gathered by centrifugation for 15 min at 1600 g. Next, the BBV particles were concentrated 40-fold by high-speed centrifugation (48 000 g at 4°C) for 40 min followed by washing with the assay buffer and homogenization with a syringe and a 30G needle. The suspension was divided into aliquots and stored at −90°C until the experiments. BBV particle preparations were done several times. Receptor concentration for the BBV particle stocks was estimated $R_{\text{stock\_UR-CG072}} = 9.7 \pm 1.1$ nM and $R_{\text{stock\_UR-MK432}} = 5.5 \pm 0.7$ nM, using the model described in [27].

2.4. Fluorescence anisotropy experiments

FA experiments were carried out on black flat bottom half-area 96 well plates (Corning, Glendale, USA). A suitable combination of the fluorescent ligand, competitive ligand and BBV particle suspension was added to each well. Assay buffer was added so that the final liquid volume in each well was 100 μl.

In saturation binding experiments, two concentrations of fluorescent ligands were used, 2 nM and 20 nM for UR-CG072 and 1 nM and 6 nM for UR-MK342. For determination of non-specific binding, 2 μM or 20 μM UNSW-MK259 were used in the case of UR-CG072 and 1 μM or 6 μM scopolamine were used in the case of UR-MK342. Two-fold serial dilutions of BBV particle suspension was added starting from 60 μl. Wells without BBV particles were used as a free fluorescent ligand control.

For competition binding experiments, the concentrations of fluorescent ligands UR-CG072 and UR-MK342 were kept constant at 5 nM, and the volume of BBV particles was also kept constant at 20 μl ($C_{\text{final}} \approx 1$–2.2 nM). Five- or six-fold serial dilutions of the competitive ligands were used. Also, replicate wells with no competitive ligand were included, and for blank correction, replicate wells with only BBV particles was included. Measurements were carried out at 3 min intervals for 13–15 h at 27°C. A custom-made glass lid was used in all the experiments to minimize the evaporation from the wells. In all cases, BBV particles were added as the last component to initiate the ligand-binding process.

For kinetic experiments, 5 nM UR-CG072 or 6 nM UR-MK342 was used. In non-specific binding wells, 6 μM or 3 μM scopolamine was added, respectively. The reaction was initiated by the addition of 20 μl of M_4 receptor displaying BBV particles. After 180 min, the dissociation was

initiated by the addition of 2 µl of 300 µM (C_{final} = 6 µM) or 150 µM (C_{final} = 3 µM) scopolamine for UR-CG072 or UR-MK342, respectively. Two-microliters of assay buffer was added instead of the competitive ligand to association kinetics wells to maintain the equivalent volume in all wells.

In all experiments, the fluorescence intensity values were blank corrected for BBV particle autofluorescence by subtracting the respective parallel or perpendicular fluorescence intensity value of a blank well from the respective measurement well. The blank wells contained no ligands but only the same concentration of BBV particles as the measurement well.

FA measurements were performed with multi-mode plate reader Synergy NEO (BioTek Instruments, Winooski, USA), which is equipped with a polarizing 530(25) nm excitation filter and 590(35) nm emission filter allowing simultaneous parallelly and perpendicularly polarized fluorescence detection. At least three individual experiments were carried out in duplicate.

2.5. Microscopy of DiI stained CHO-K1-hM$_4$R cells

CHO-K1-hM$_4$R cells were grown as described above and seeded with a density of 25 000 cells per well into a µ-Plate 96 well Black plate (Ibidi, Gräfelfing, Germany) 5 h before the experiment. A stock solution of 1 mM 1,1′-dioctadecyl-3,3,3′,3′-tetramethylindocarbocyanine perchlorate (DiI) (Invitrogen, Eugene, Oregon, USA) in DMSO stored at −20°C was thawed and sonicated in an ultrasound bath for 5 min to disrupt aggregates. Cell medium was removed and replaced with 200 µl per well of 2 µM DiI in Dulbecco's phosphate-buffered saline (DPBS) with Mg^{2+} and Ca^{2+} (Sigma-Aldrich) to stain the cell membranes. The cells were incubated with the solution for 10 min before imaging. The cells were imaged with Cytation 5 cell imaging multi-mode plate reader equipped with 20X LUCPLFLN objective (Olympus) from Bright-field and RFP channels (LED light source with excitation filter 531(40) nm and emission filter 593(40) nm for RFP channel (BioTek Instruments) with the following parameters for bright-field: LED intensity = 4, integration time = 110 ms, camera gain = 24 and for RFP fluorescence channel: LED intensity = 1, integration time = 71 ms, camera gain = 24. The cells were imaged in the montage mode (196 locations) with Z-stack (10 planes, 4 planes below and 5 planes above focus) to cover any imaging location-dependent variability and simulate potential autofocusing errors.

2.6. Live-cell ligand-binding imaging

CHO-K1-hM$_4$R cells were seeded into µ-Plate 96 well Black plate (Ibidi) at densities of 25 000–55 000 cells per well in DMEM/F-12 medium and incubated for 5–7 h. Immediately before the measurement, the cell culture media was exchanged for the same cell culture media containing ligands. At all times, the well volume was kept at 200 µl.

For determining UR-CG072 affinity to the M$_4$ receptor, saturation binding experiments were carried out using twofold dilutions of UR-CG072 starting from 8 nM. Non-specific binding was measured in the presence of 3.7 µM scopolamine. The cells were incubated with ligands in Cytation 5 at 5% CO_2 and 37°C for 2 h before imaging.

For measuring UR-CG072 binding kinetics to M$_4$ receptor, 2 nM UR-CG072 was added to the cells, and imaging was immediately initiated. To achieve sufficient temporal resolution,

only two wells were imaged in parallel. After approximately 3 h of association, 10 µl of 100 µM scopolamine (C_{final} = 5 µM) was added to start dissociation.

The competition binding assay was performed using 2 nM UR-CG072. The different competitive ligand concentrations were pipetted to the plate in randomized order to avoid a correlation between well imaging order and concentration. It was determined that 2 h was sufficient to reach equilibrium for IC$_{50}$ value measurement as the IC$_{50}$ values for scopolamine and carbachol at 2 and 5 h remained constant within uncertainty limits.

The imaging was performed with Cytation 5 as described above. Saturation binding experiments were performed with following imaging parameters in bright-field: LED intensity = 4, integration time = 110 ms, camera gain = 24 and in RFP fluorescence channel LED intensity = 1 or 2, integration time = 827 ms, camera gain = 24. For kinetic binding assays all the parameters were the same except for RFP fluorescence channel LED intensity = 5. For competition binding assays the imaging parameters used in bright-field were: LED intensity = 5, integration time = 1222 ms, camera gain = 0 and in RFP fluorescence channel: LED intensity = 5, integration time = 613 ms, camera gain = 24 or the same as for kinetic experiments. The cells were imaged in the montage mode (4 locations per well) with Z-stack (10 planes, 4 planes below focal plane, 1 in focus and 5 planes above focal plane).

2.7. Cell segmentation with ilastik software

To develop a bright-field cell segmentation model based on the random forest (RF) algorithm, a total of three ilastik [53] pixel classification models were trained: RF-FL-1 (random forest-based fluorescence image cell segmentation), RF-BF-1 (random forest-based bright-field image cell segmentation model version 1) and RF-BF-2 (random forest-based bright-field image cell segmentation model version 2). Two of the models (RF-FL-1 and RF-BF-1) were intermediate helper models used for training the final RF-BF-2 model. Here, the models are named by combining the model type (RF or U-Net3), an input imaging modality that the model used for cell detection (BF for bright-field images and FL for fluorescence images), followed by the index of the model of the particular type. For developing the RF-FL-1 model, a set of fluorescence images of CHO-K1-hM$_4$R cells stained with fluorescent lipophilic dye DiI was generated. Thirty of these images were randomly chosen from different locations of the well for the training set. The images were in-focus (10 images), 3 µm above (10 images) or 3 µm below (10 images) the focal plane to increase the model robustness against focusing errors. The Gaussian smoothing, Laplacian of Gaussian, Gaussian gradient magnitude, difference of Gaussians, structure tensor eigenvalues and Hessian of Gaussian eigenvalues features were selected for sigma values of 0.70, 1.00, 1.60, 3.50, 5.00, 10.00, 15.00 and 20.00 pixels. In addition, the Gaussian smoothing feature with a sigma value of 0.30 pixels was selected in the ilastik feature selection stage. RF-FL-1 was set up to perform binary pixel classification using cell and background classes. Some pixels of cells and background were manually annotated by adding annotations over the respective pixels of the in-focus images. More annotations were added at the fringe of cells to enhance the accuracy of the predictions. The annotations of the in-focus images were transferred to the respective out-of-focus images from the same field of

Table 1. Quality metrics of the developed machine-learning models.

| metric	model				
	U-Net3-FL-1	RF-FL-1	U-Net3-BF-1	RF-BF-1	RF-BF-2
recall	0.94	0.91	0.86	0.75	0.72
precision	0.88	0.94	0.93	0.77	0.74
F_1 score	0.91	0.93	0.89	0.76	0.73
MCC	0.89	0.91	0.86	0.71	0.67

view. With these annotations, the RF-FL-1 was trained. Model export was set to generate simple binary segmentation. Then, the cells on the rest of the fluorescence images (186 images) were segmented in the batch processing mode creating a set of masks for 196 fields of view with the ten fields of view remaining in the training set. Next, the binary segmentation images were automatically reclassified into three classes: intracellular area (IC), membrane (MB) and near-membrane background (NMBG) with the rest of the pixels representing background (BG). IC class was generated by image erosion of the predicted cell masks by a 2-pixel radius disk structuring element. MB class was generated by image dilation of IC masks with a 3-pixel radius disk structuring element and pixels were assigned to the NMBG class by further image dilation of the MB images with a 7-pixel radius disk structuring element and excluding pixels already assigned to MB or IC classes. Next, a class balancing step was performed to obtain an equal number of pixels (MBs) for each of the classes. For that, all of the pixels from the class with the smallest MBs were selected and an equal MBs were selected randomly from IC and NMBG classes. The operation was performed for each image separately. Images generated by this process were considered as the ground truth for training RF-BF-1 model. RF-BF-1 was trained to detect cells from contrasted projections of bright-field Z-stacks. The Z-stack of bright-field images was converted into a single higher contrast image as described in [35]. Twenty fields of view were used as a training set in RF-BF-1 for the detection of IC, MB, NMBG areas from the contrast-enhanced bright-field image projections. The Gaussian smoothing, Laplacian of Gaussian, Gaussian gradient magnitude, difference of Gaussians, structure tensor eigenvalues and Hessian of Gaussian eigenvalues features were selected for sigma values of 0.70, 1.00, 1.60, 3.50, 5.00, 10.00, 15.00, 20.00, 25.00, 30.00 and 35.00 pixels. In addition, the Gaussian smoothing filter with a sigma value of 0.30 pixels was selected in the ilastik feature selection stage. Twenty ground truth images generated by RF-FL-1 were used as labels of IC, MB, NMBG classes in the respective images to train a model for the detection of three classes of pixels from the contrast-enhanced bright-field images. The prediction quality was estimated by the recall, precision, F_1 score and Matthews correlation coefficient (MCC) metrics as shown in table 1. Classification quality metrics were measured by considering the IC pixels to form a positive class while all other classes (MB, NMBG, BG) were merged to form the negative class. Thus, misclassifications of pixels between MB, NMBG and BG classes had no impact on the quality metrics.

Finally, the RF-BF-2 model was trained to improve the prediction quality of the RF-BF-1 model by adjusting the class balance by adding ground truth annotation to pixels

that the RF-BF-1 model had failed to classify. The same training set of 20 contrast-enhanced bright-field images was used for the RF-BF-1 model. In this training run, the fourth class of pixels was created for BG from all the previously unclassified pixels. To create ground truth images for RF-BF-2, the class balancing step was performed again as previously described. Additionally, the labels were improved by manually adding pixels to each class, which the RF-BF-1 model had failed to classify. The same image features were used as in the RF-BF-1 model. The prediction quality of RF-BF-2 was evaluated with the test set (table 1 and figure 7g). By visual inspection, the addition of extra labels removed the largest and clearest misclassifications (figure 7f,g) and the ones remaining were overlapping with areas where the volume of training data was already large. As overall image detection parameters were not better for RF-BF-2 compared to RF-BF-1 (table 1), it was deemed that the model quality had reached a plateau, and further addition of data would not provide any significant model generalization. The model development pipeline is presented on figure 1a.

2.8. Cell segmentation with deep learning

For training the models for the DL pipeline, ten in-focus RFP fluorescence channel images of CHO-K1-hM$_4$R cells stained with DiI dye were manually labelled using the ilastik pixel classification pipeline user interface. For that, pixels were classified as either cells or background. The manually generated annotations were exported. Next, a background correction step was used to remove systematic illumination differences from the fluorescence images. The ten images along with corresponding ground truth annotations were randomly sampled into training, validation and test sets as follows: six images in the training set, two images in the validation set and two images in the test set. The training and validation set images were cropped to the input size of the U-net (288×288 pixels) and augmented using a sequential augmenter with the augmentations (rescaling 0–5%, shearing 0–1 pixels, piecewise affine shearing 1–5%, random rotation ±45°, random left–right flip 50% probability and random up-down flip 50% probability) using the imgaug library [54]. A total of 6000 training tiles and 2000 validation tiles were generated (1000 augmented tiles of each image). The U-Net inspired fully convolutional U-Net3 architecture (figure 1c) was used to train a model, U-Net3-FL-1 (U-Net3 architecture-based fluorescence image cell segmentation), for cell detection from the fluorescence images [47,49]. The training was carried out using the following parameters: Adam optimizer [55], learning rate = 0.0002, beta 1 = 0.9, beta 2 = 0.999, epsilon = 10^{-8}, number of epochs = 20, loss
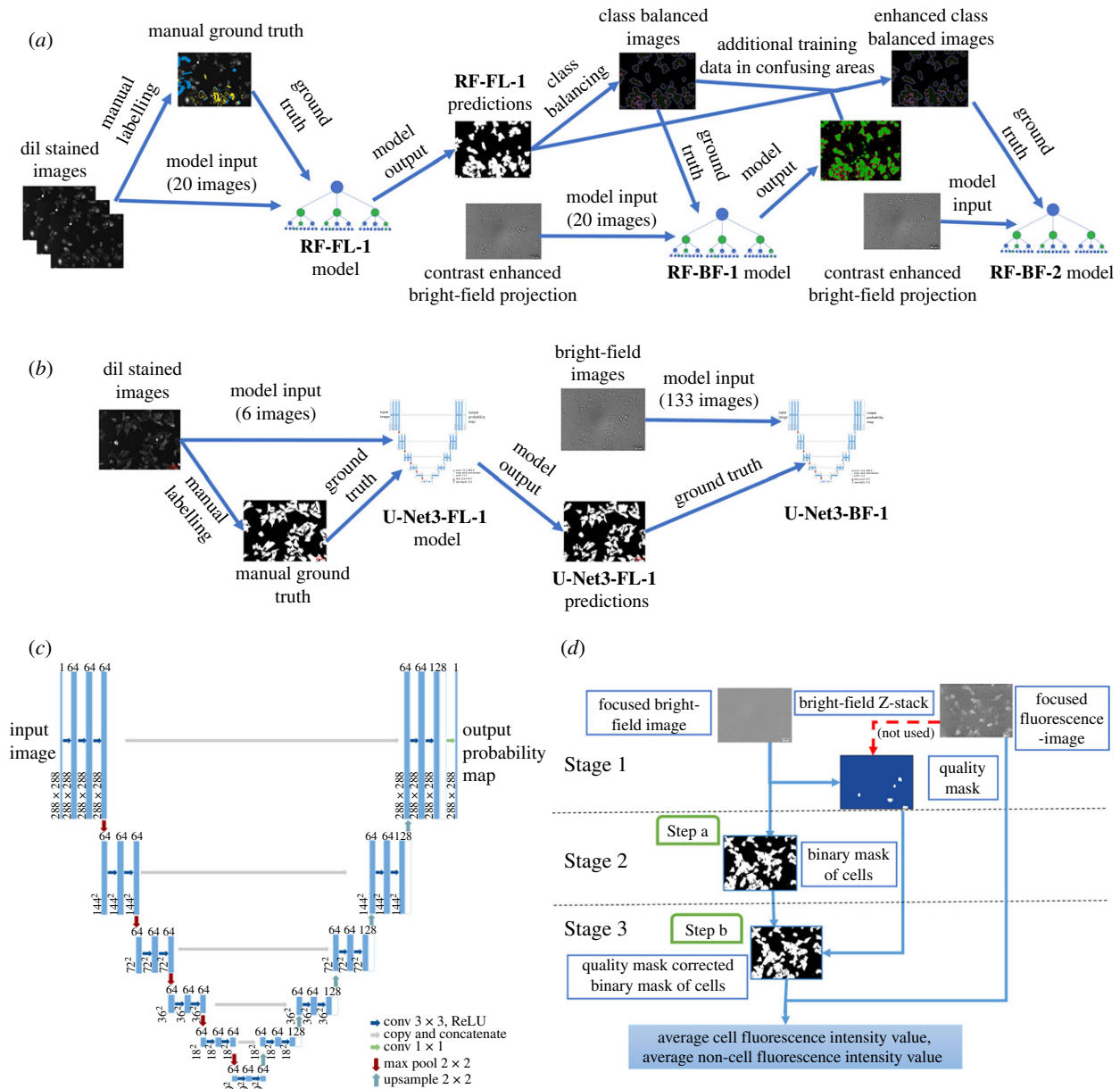
Figure 1. The architecture of the image analysis pipelines. (*a*) For training the random forest-based RF-BF-2 model, a training pipeline was used which also generated the helper models RF-FL-1 and RF-BF-1. (*b*) For training the U-Net3-BF-1 model the training pipeline was used which also generated the helper model U-Net3-FL-1. (*c*) U-Net type architecture was used for the DL pipeline. (*d*) The cell detection pipeline using the trained models was implemented in Aparecium MembraneTools module. In this pipeline, Stage 1 corresponds to data pre-processing, Stage 2 to cell segmentation and Stage 3 to data post-processing. In (*a*), the U-Net3-BF-1 model is used and in (*b*) the binary mask is corrected with the quality mask.

function = binary cross-entropy. The validation set loss was confirmed to have reached a minimum within 20 epochs. The model quality was assessed for the test set images. Next, the model was used to predict the masks for 191 DiI labelled fluorescence images. These images were again separated into training, validation and test sets along with the corresponding in-focus bright-field images of the same fields of view (133, 29 and 29 images, respectively). The focal plane had been manually chosen in a prior step. As it has been previously shown that similar DL network architectures require considerably more bright-field data to converge to an optimal solution compared to fluorescence data, a different strategy was chosen for training DL for cell detection from bright-field images [40,49,56]. As the training data volume was substantially larger, a data generator was used for cropping the images to the correct size (288×288 pixels) instead of predefined training and validation sets. A batch size of eight images was used during training.

No augmentation was used for bright-field data. The same model architecture was used for the U-Net3-BF-1 (U-Net3 architecture-based bright-field image cell segmentation) model as for U-Net3-FL-1. In this training run, early stopping with patience = 20 was used, the model converged after 90 epochs. Also, learning rate reduction with a factor of 0.1 and patience = 10 was used. All other parameters were the same as for the fluorescence-based model. The final model U-Net3-BF-1 was used to predict the segmentation of the test set and equivalent metrics were calculated (table 1). The model development pipeline is presented on figure 1*b*.

2.9. Image analysis pipeline

To carry out cell segmentation from all microscopy images, a suitable image analysis pipeline was developed. For using ilastik based models, the same pipeline was used as in [35] with minor modifications. The ilastik segmentation label

index was updated according to the RF-BF-1 model design (segmentation label index = 2) and morphological corrections were not used as it was not necessary for whole-cell segmentation in contrast to contour segmentation.

For using the U-Net3-BF-1 model for prediction, the *MembraneTools* module of Aparecium data and image analysis software (https://gpcr.ut.ee/aparecium.html) was updated to be able to use Keras framework [57] models for prediction. Unlike for RF-BF-1, for U-Net3-BF-1 only a single in-focus bright-field image was used for input instead of the contrast-enhanced image generated from bright-field Z-stacks. As the U-Net3-BF-1 model can predict only the 288×288-pixel patches, the bright-field images are tiled before prediction and the predictions are later stitched to original size images (figure 1d, step a).

The quality mask was manually generated (figure 1d, stage 1) as previously described [35] and areas of low quality were removed from image quantification (figure 1d, step b).

For fluorescence image quantification, the in-focus fluorescence image was selected from the Z-stack manually and the image intensity was calculated only for the areas detected as cells by the segmentation model.

2.10. Software performance tests

During software performance tests ilastik v. 1.3.3post3 and MATLAB (The MathWorks, USA) v. R2021a were used on a PC with 16 GB RAM, i7–10750H CPU (2.6 GHz) with 6 cores. DL pipeline inference was run on Nvidia Quadro T1000 GPU. For training the DL models the High Performance Cluster of University of Tartu was used [58].

2.11. Pharmacological data analysis

Aparecium 2.0 software was used to blank the raw parallel and perpendicular intensity values and calculate the FA values using the formula [59]:

$$FA(t) = \frac{I(t)_{\mathrm{II}} - I(t)_{\perp}}{I(t)_{\mathrm{II}} + 2 \cdot I(t)_{\perp}}, \tag{2.1}$$

where $I(t)_{\mathrm{II}}$ is the parallel fluorescence intensity and $I(t)_{\perp}$ is the perpendicular fluorescence intensity at time point t.

K_i values were calculated with the Cheng–Prusoff equation [60], using the IC_{50} values gained from data fitting with GraphPad Prism 5.0 (GraphPad Software, San Diego, USA) with a three-parameter logistic regression model (log(inhibitor) versus response).

For calculation of kinetic parameters k_{on}, k_{off} and $K_{d\_kinetic}$ of the microscopy data, GraphPad Prism 5.0 'Association then dissociation' model was used. K_d calculation form microscopy data was also done with GraphPad Prism 5.0, but the model used was 'one site—total and non-specific binding'.

For K_d calculation from FA data a global model form [27], which takes ligand depletion into account was used. To calculate k_{on}, k_{off} and $K_{d\_kinetic}$ from FA kinetic data a modified version of IQMTools/SBToolbox2 (IntiQuan, Basel, Switzerland) was used to fit FA values with the previously published model [17]. The model assumes four possible interactions: the interaction between the receptor (R) and the fluorescence ligand (L), the receptor and the competitive unlabelled ligand (C), non-specific binding sites from the receptor preparation (NBV) and fluorescent ligand, the interaction between non-specific binding sites on the microplate

(N) and the fluorescent ligand. The corresponding reactions can be described by the following schemes:

$$R + L \rightleftarrows RL,$$
$$R + C \rightleftarrows RC,$$
$$NBV + L \rightleftarrows NBVL$$
$$and \quad N + L \rightleftarrows NL$$
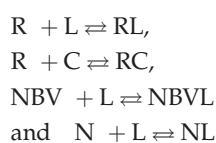
The concentrations in this model are connected to the predicted FA values through the equation:

$$FA(t) =$$
$$\frac{\{RL\}_t \times FA_{RL} + \{L\}_t \times FA_L + \{NL\}_t \times FA_{NL} + \{NBVL\}_t \times FA_{NBVL}}{\{RL\}_t + \{L\}_t + \{NL\}_t + \{NBVL\}_t}, \tag{2.2}$$

where $\{RL\}_t$, $\{L\}_t$, $\{NL\}_t$ and $\{NBVL\}_t$ are the instantaneous concentrations of RL, L, NL and NBVL, respectively, at timepoint t, and FA_{RL}, FA_L, FA_{NL} and FA_{NBVL} are the intrinsic fluorescence anisotropies of the RL, L, NL and NBVL states, respectively.

All the uncertainties given are weighted standard error of the mean of at least three independent experiments if not stated otherwise.

2.12. Statistical analysis

For determining the quality of all machine-learning cell detection models, four metrics were considered:

$$Recall = \frac{TP}{TP + FN}, \tag{2.3}$$

$$Precision = \frac{TP}{TP + FP}, \tag{2.4}$$

$$F_1 \ score = \frac{2 * TP}{2 * TP + FP + FN} \tag{2.5}$$

and

$$MCC = \frac{TP * TN - FP * FN}{\sqrt{(TP + FP) * (TP + FN) * (TN + FP) * (TN + FN)}}, \tag{2.6}$$

where true positive (TP) denotes the number of correctly detected pixels belonging to cells, true negative (TN) is the number of correctly predicted pixels not belonging to cells, false positive (FP) is the number of non-cell pixels detected as cells, false negative (FN) is the number of cell pixels detected as non-cell pixels.

To compare U-Net3-BF-1 and RF-BF-2 model qualities for determining IC_{50} values from the live-cell microscopy assay, the R^2 of the nonlinear fits were compared in a pairwise manner using one-tailed Mann–Whitney U-test in GraphPad Prism 5.0 assuming that U-Net3-BF-1 is the superior model.

To determine the assay suitability for HTS applications, Z' values were calculated according to the formula [61]:

$$Z' = 1 - \frac{3(\sigma_{bottom} + \sigma_{top})}{|\mu_{bottom} - \mu_{top}|} \tag{2.7}$$

where σ_{top} and σ_{bottom} represent the standard deviations of blank wells (negative controls) and wells with a full displacement of the fluorescent ligand (positive controls), respectively. μ_{top} and μ_{bottom} correspond to means of negative and positive controls, respectively. The values from individual experiments were normalized to the respective top and bottom plateau values for each concentration-response curve separately to remove batch-to-batch variation effects of the receptor source.
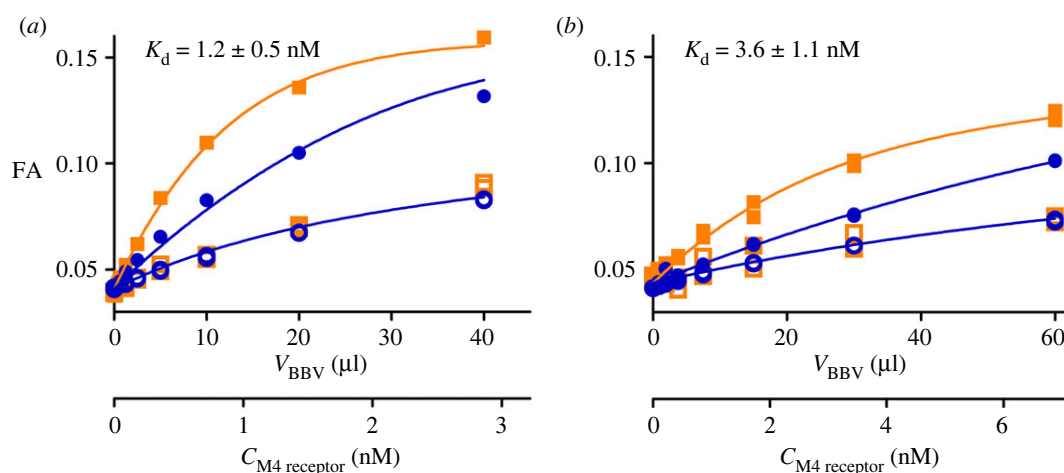
Figure 2. Binding curves of fluorescent ligand binding to M_4 receptor. 1 nM (squares) or 6 nM (circles) UR-MK342 (*a*) or 2 nM (squares) or 20 nM (circles) UR-CG072 (*b*) incubated with different concentrations M_4 receptor. Total binding (filled symbols) was determined in the absence and non-specific binding (open symbols) in the presence of 1000-fold excess of UNSW-MK259 in the case of UR-CG072 or scopolamine in the case of UR-MK342. The 1 h measurement point for UR-CG072 and 5 h measurement point for UR-MK342 are shown and was used for calculations. The concentration of M_4 receptor binding sites ($C_{M4\ receptor}$) was calculated post hoc from the results of these experiments using the model described in [27]. A representative experiment of at least three independent experiments is shown. Experiments were performed in duplicates with all measurement data points shown.

3. Results

3.1. Determination of binding affinities of UR-CG072 and UR-MK342 to M_4 receptor displayed in BBV particles with FA

The FA method used here allows continuous measurement of receptor-fluorescence ligand complex formation or dissociation. FA depends on the ratios of free and bound fluorescence ligand states (equation (2.2)). The specific FA values of each state depend on the fluorescence lifetime as well as the rotational freedom of the fluorophore in the corresponding state. To observe significant changes in FA signal it is necessary that the mole ratios of both the free and bound fluorescence ligand change when receptor concentration, total fluorescence ligand concentration, competitive ligand concentration, time, or a combination of these factors is varied. This is best achieved when concentrations of the probe and its target protein are kept close to their binding K_d.

For these reasons, only certain fluorescence ligands with suitable fluorophores and binding affinities, usually from low picomolar to low nanomolar ranges, are considered as probe candidates for FA assay. Two 5-TAMRA labelled ligands, UR-CG072 and UR-MK342 from [16], were chosen for the development of FA assays due to a suitable label and high affinity to M_4 receptor determined by radioligand binding to whole cells.

First, the saturation binding experiments were carried out to determine fluorescence ligand-binding affinities to M_4 receptors displayed on BBV particles. Both ligands showed similar and high binding affinity ($K_{d\_UR-CG072} = 3.6 \pm 1.1$ nM, $K_{d\_UR-MK342} = 1.2 \pm 0.5$ nM; figure 2) which are in good agreement with the radioligand binding values ($K_{i\_UR-CG072} = 3.7 \pm 0.6$ nM, $K_{i\_UR-MK342} = 0.97 \pm 0.07$ nM [16]). However, UR-MK342 binding has a larger dynamic range of FA values compared to UR-CG072. The same tendency was also found in FA assays with the M_2 receptor [17]. As the effect is evident

for both receptor subtypes, it might be attributed to the more flexible linker in UR-CG072. Nevertheless, high affinity and sufficient dynamic range mean that both ligands would be suitable for kinetic measurements as well as using these as probes for measuring competitive ligand-binding parameters.

Next, the ligand-binding kinetics of UR-CG072 and UR-MK342 to the M_4 receptor were studied. In contrast to similar affinities, the kinetic properties of UR-CG072 and UR-MK342 were quite different (figure 3). The faster association and dissociation kinetics of UR-CG072 make it more suitable for FA-based screening assays as this allows increasing the assay throughput by shortening the incubation times which reduces problems concerning potential receptor source sedimentation, liquid evaporation or even degradation of the ligands or the receptor [62]. Faster kinetics is also beneficial for live-cell microscopy assays, where too long experiments can lead to problems with cell culture such as detachment and changes in medium composition.

3.2. Affinity screening a panel of MR ligands with UR-CG072 and UR-MK342

Fluorescence ligands are often applied for determining the affinities of unlabelled ligands. Therefore, the suitability of both ligands was studied as reporter probes in competition with unlabelled M_4 receptor ligands. For that, a panel of common M_4 receptor ligands was chosen such that the expected affinities would cover a wide range of values and contain both agonists and antagonists. In addition, some unlabelled ligands, which are structurally similar to the fluorescence ligands [50,51,63], were chosen to assess the assay's ability to work with dualsteric compounds. The set of ligands was investigated in competition binding experiments with both UR-CG072 and UR-MK342 (figure 4).

Both fluorescent ligands can successfully be used as reporter ligands with a high signal-to-noise ratio and very good Z-prime ($Z'_{UR-CG072} = 0.52$, $Z'_{UR-MK342} = 0.67$) making
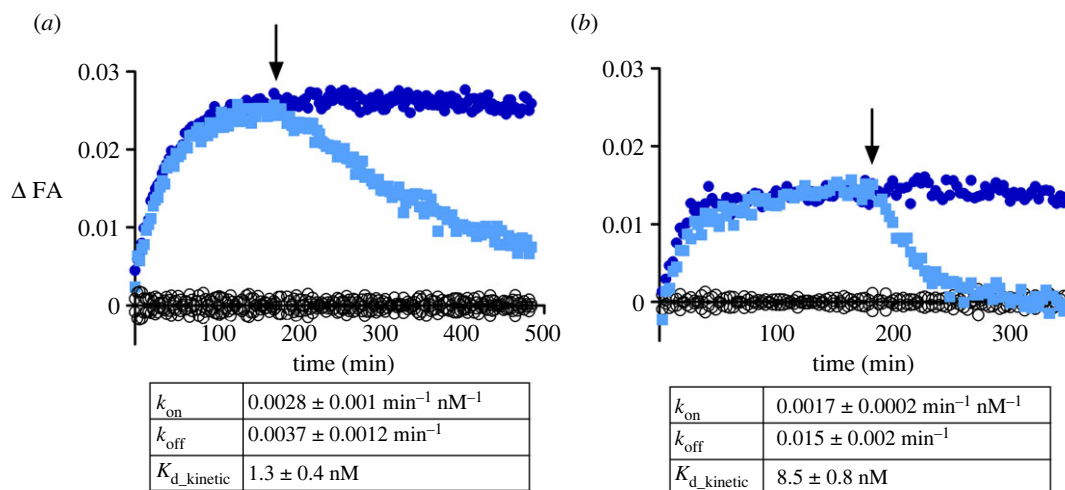
Figure 3. Time course of FA change caused by UR-MK342 (a) or UR-CG072 (b) binding to M_4 receptors on the BBV particles. The reaction was initiated by the addition of 20 µl M_4 receptor displaying BBV particles to 6 nM UR-MK342 (a) or 5 nM UR-CG072 (b) in the absence (open blue square, filed blue circle) or presence (open black circle) of 6 µM (a) or 3 µM (b) scopolamine, respectively. After 180 min (indicated with an arrow) dissociation was initiated by the addition of 6 µM (a) or 3 µM (b) scopolamine (open blue square). An equivalent volume of assay buffer was added to association controls (filed blue circle). Representative experiments of at least three independent experiments are shown. ΔFA is calculated by subtracting the FA value of non-specific binding from the measured FA value of the corresponding measurement.
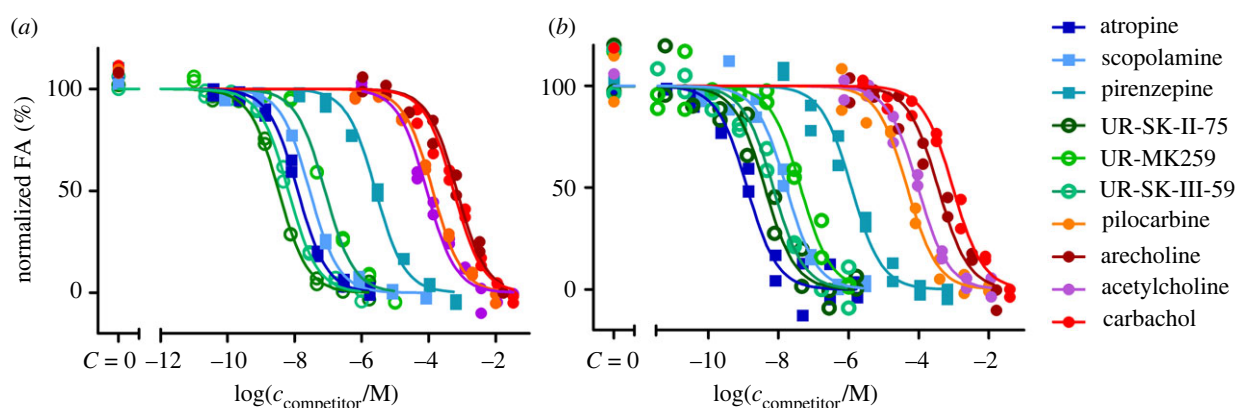
Figure 4. FA-based M_4 receptor competition binding experiments performed with 5 nM UR-MK342 (a) or 5 nM UR-CG072 (b) and reported muscarinic M_4 receptor ligands. BBV particles displaying the M_4 receptors (V(BBV) = 20 µl) were used as the receptor source. The 9 h measurement point is shown and used for analysis for all ligands. From the used competitive ligands, acetylcholine, carbachol, arecoline, pilocarpine are agonists, scopolamine, atropine, pirenzepine, UNSW-MK259, UR-SK75 and UR-SK59 are antagonists. A representative experiment of at least three independent experiments performed in duplicates is shown. Normalization was performed by taking the upper plateau value as 100% and lower plateau value as 0% separately for each displacement curve.

the assay compatible with HTS formats which generally require a minimum Z' of 0.5. However, as UR-CG072 has faster kinetics than UR-MK342, a longer incubation time is needed to determine the competitive ligand affinity using UR-MK342. To avoid possible under-or overestimation of IC_{50} values, it is important to wait until the equilibrium is reached [23].

To make the measurement values comparable, the pK_i values were calculated from the IC_{50} value for each ligand using the Cheng–Prussoff equation. While not all assumptions of the Cheng–Prussoff equation [60] are fulfilled, it has been previously shown that with these ligands the potential systematic error introduced by this operation is relatively small [17]. pK_i values obtained from experiments using the two different reporter ligands correlated very well ($R^2 = 0.96$), and the linear regression slope of the obtained pK_i values with both probes is very close to unity (0.97 ± 0.04) while the intercept is close to zero (0.3 ± 0.3) (figure 5a).

This validates that both probes can be used to determine the unlabelled ligand affinities in the FA assay.

Out of the tested ligands, UNSW-MK259, which represents the non-labelled analogue of UR-CG072, had the largest deviation from the best regression line (figure 5). The reason for this deviation is unknown but may be connected to potential dualsteric binding modes of UNSW-MK259, UR-MK342 and UR-CG072, which could alter the binding mechanism. However, explaining this effect remains the topic of future studies.

3.3. Adjusting live-cell microscopy assay for measuring UR-CG072 binding to M_4 receptor

To keep the cells viable and with normal morphology during imaging experiments, it is necessary to maintain specific conditions, like 5% CO_2, 37°C, and sufficient nutrient concentrations in the media. These parameters may start to
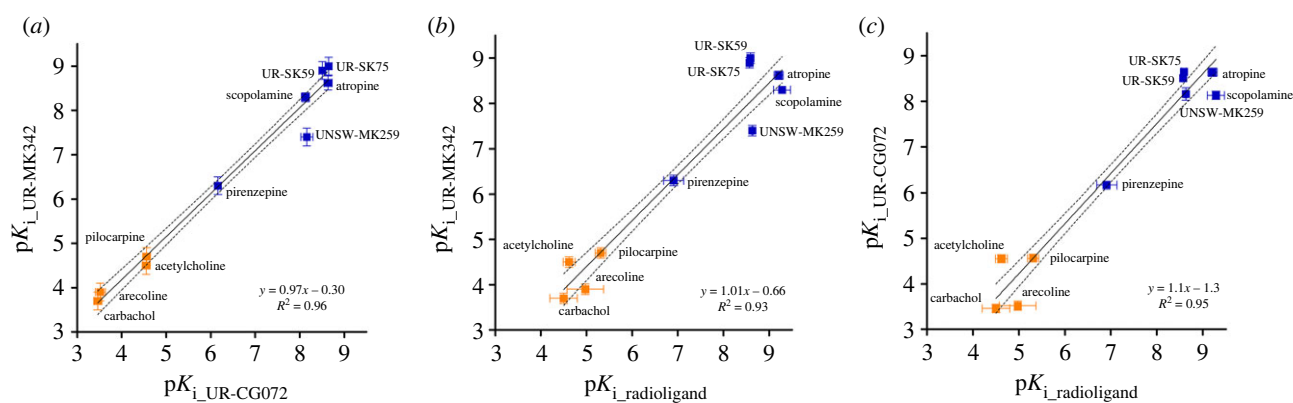
Figure 5. Correlations of binding affinities (pK_i values) of ligands to M_4 receptor, measured with different probes and assays. (*a*) FA assays with UR-CG072 and UR-MK342. (*b*) FA assay with UR-MK342 and radioligand binding (literature data). (*c*) FA assay with UR-CG072 and radioligand binding (literature data). Investigated agonists are presented as orange symbols (filled orange square), antagonists as blue symbols (filled blue square). Black lines represent the linear regression between the datasets, and the dashed black lines represent the 95% confidence bands. Data shown for FA are the mean of at least three independent experiments, and the error bars represent s.e.m. Data shown for radioligand are the mean of values from articles shown in table 3, and the error bars represent s.e.m. of these data.
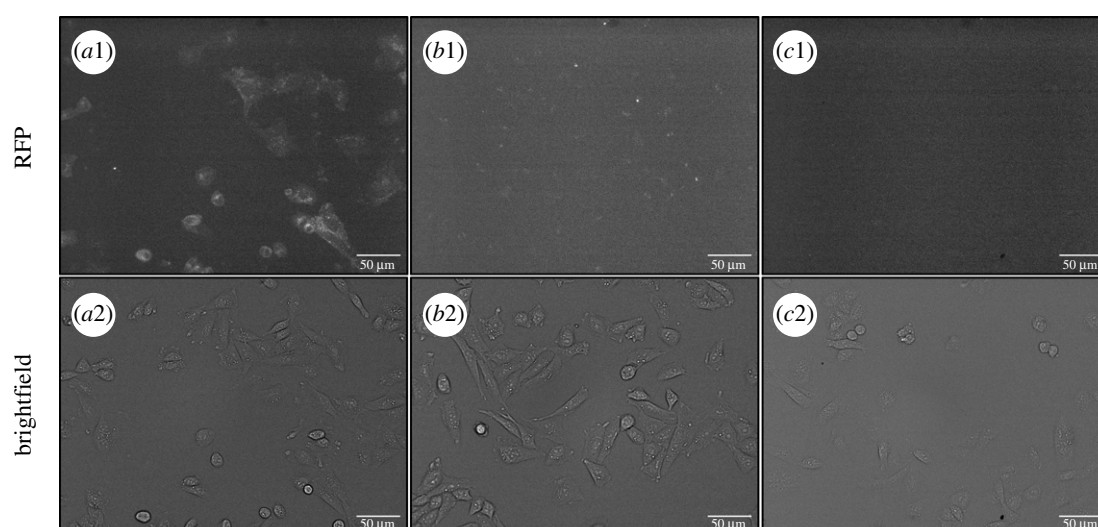

	(a1)(a2)	(b1)(b2)	(c1)(c2)
CHO-K1-hM$_4$R	+	+	−
CHO-K1	−	−	+
scopolamine	−	+	−

Figure 6. Fluorescence microscopy images (top row) and corresponding bright-field images (bottom row) of UR-CG072 binding to CHO-K1 cells. Either wild-type CHO-K1 cells (*c*1 and *c*2) or CHO-K1-hM$_4$R cells (*a*1, *a*2, *b*1, *b*2) in DMEM/F12 medium with added 9% FBS and antibiotic antimycotic solution were incubated with 2 nM UR-CG072 in the absence (*a*1, *a*2, *c*1, *c*2) or presence (*b*1, *b*2) of 5 µM scopolamine for 3 h. The number of seeded cells per well was 30 000. The contrast of fluorescence images was enhanced for presentation purposes only, the same lookup table was used for all images. The scale bar corresponds to 50 µm.

drift over long periods. Therefore, UR-CG072 was selected for the live-cell assay due to its faster binding and dissociation kinetics. First, it was confirmed that the binding of 2 nM UR-CG072 to CHO-K1-hM$_4$R cells can be detected by fluorescence microscopy (figure 6*a*1). For non-specific binding controls, a similar experiment was performed in the presence of 5 µM scopolamine. As illustrated in figure 6 there is a significant difference in fluorescence intensity between total binding (figure 6*a*1) and non-specific binding (figure 6*b*1). To confirm that all the signal is specifically caused by ligand binding to M_4 receptors, the binding of 2 nM UR-CG072 to CHO-K1 cells not expressing M_4 receptor was measured. Under these conditions, there was no detectable accumulation of UR-CG072 to CHO-K1 cells (figure 6*c*1).

The results show that the differences between cell contour and cell body fluorescence intensities are smaller for the flatter CHO-K1 cells compared to HEK293 cells used in a previous study [35], which are elongated in the Z-direction. Therefore, it is necessary to analyse the fluorescence intensity of the whole cell body, which introduces an increased proportion of cell autofluorescence to the signal. Moreover, the imaging experiments were carried out in nutrient-rich cell culture media rather than DPBS buffer, as is suggested in [35]. This removes the need for more expensive special imaging media but increases background fluorescence levels. Combining these effects with using 5-TAMRA fluorophore instead of Cy3B as was used in [35], the overall signal level was greatly reduced in this assay compared to the previous one. However, as biological variability is still the main contributor to the assay uncertainty, reducing such variability at the cost of a reduced signal is still beneficial to the overall assay quality.
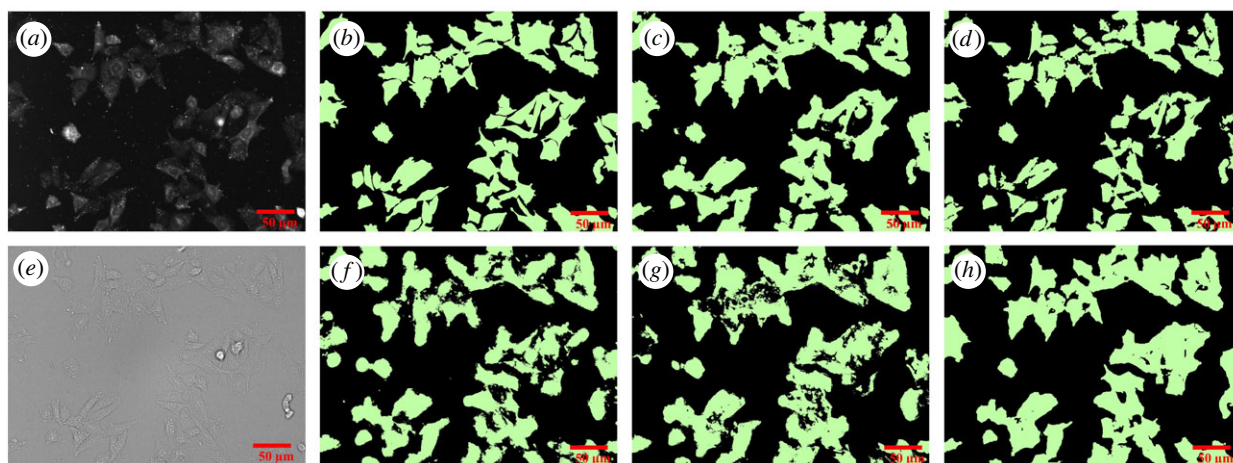
Figure 7. Microscopy images and corresponding binary masks of CHO-K1-hM$_4$R cells stained with DiI. The top row shows cell detection from the fluorescence image (*a*) by manual segmentation (*b*), RF-FL-1 model (*c*) and U-Net3-FL-1 (*d*). The bottom row shows cell detection from the bright-field image (*e*) by RF-BF-1 model (*f*), RF-BF-2 model (*g*) and U-Net3-BF-1 (*h*). The scale bar corresponds to 50 μm.

These images also reveal that the amount of M$_4$ receptors on the cell membrane surface in all cells is different and that in some cells ligand binding could not be detected at all (figure 6 *a*1,*a*2). This aspect should be considered when moving on to single-cell-based quantification using this particular cell line. However, the current microscopy method averages the signal from a large number of cells and all cells used on a single assay day are seeded from the same population. Furthermore, the absolute intensity values have no direct or systematic influence on the calculated ligand-binding parameters (K_d, k_{on}, k_{off} and K_i) and only lead to lowered signal-to-noise ratio. While a higher signal-to-noise ratio is beneficial in general, in the current case, it only has a limited impact on the overall measurement uncertainty.

3.4. Comparison of random forest and deep learning-based image analysis pipelines

Since the morphologies of HEK293 cells and CHO-K1 cells and the fluorescence probes are different, it was necessary to adjust the original pipeline previously developed for HEK293 cell analysis [35]. Due to a lower contour contrast of CHO-K1 cells compared to HEK293 cells, it was necessary to quantify the fluorescence intensity from the entire cell mask instead of only the cell contours.

A second adjustment to the original pipeline was needed due to the lower apparent brightness of the ligand–receptor complex. While the NAPS-Cy3B fluorescence signal in the dopamine D$_3$ receptor system was close to twice as high as the image background intensity [35], the signal of CHO-K1-hM$_4$R bound UR-CG072 was only 4% above the background signal. Due to the high absolute signal level in the D$_3$ receptor system, it was not necessary to find the in-focus fluorescence plane in the original pipeline and instead the maximum intensity projection of the Z-stack could be used. In the current case, this approach is not suitable and leads to complete signal degradation (data not shown). Therefore, the fluorescence intensity must be quantified from the highest quality focal plane.

Improvements were also introduced into the model development and ground-truth generation process. The original pipeline relied on a human analyst to detect cell contours

from bright-field images. Even though it was necessary to perform this step only once, it required significant manual labour and detecting cell contours from bright-field images is still more difficult compared to detection from fluorescence images. To address these issues, another approach was pursued. The cell membranes were stained with a lipophilic dye DiI and then imaged in both fluorescence and bright-field channels. For a small number of fluorescence images, cell masks were manually drawn. Next, machine-learning models RF-FL-1 and U-Net3-FL-1 were trained to generate cell masks from the DiI stained fluorescence images. These models were in turn used to predict the masks from a larger dataset of fluorescence images. The prediction masks then served as slightly lower quality, but significantly higher quantity ground truth for the next set of models (RF-BF-1, RF-BF-2 and U-Net3-BF-1), which predict the cell masks from bright-field images. The same conceptual approach was successful for training both the RF-based pipeline implemented in ilastik as well as the U-Net3 based DL pipeline developed using Jupyter notebooks [64] and Keras DL framework [57]. Considering all the aspects, both developed pipelines were superior to the original pipeline from the pipeline development perspective with a significantly reduced amount of manual annotation required.

3.5. Prediction quality comparison

The prediction quality of the DL models and ilastik based RF model were compared to determine the most suitable pipeline for analysis (figure 7 and table 1). Visually, all models can segment most of the cells from the bright-field images with good quality. The main difference between the models is that U-Net3-BF-1 (figure 7*h*) produces cells with more consistent and smooth shapes, similar to the ground truth (figure 7*b*) while RF-BF-2 (figure 7*g*) creates rugged edges and also detects many small fragmented objects far from the cells. Numerically, the quality of bright-field detection (table 1, F_1 score = 0.89) is somewhat lower than the current state of the art solutions in the cell tracking challenge [65] when compared to the most similar dataset of DIC-HeLa cells (F_1 score = 0.93) [65–68]. However, it must be noted that such small differences could be easily caused by differences in imaging modes, magnifications, cell line morphology or amount of training data

among other parameters. The F_1 score of the fluorescence image-based predictions of both U-Net3-FL-1 (figure 7d) and RF-FL-1 (figure 7c) are already substantially lower than unity. At the same time, the U-Net3-BF-1 model has only slightly lower quality metrics compared to U-Net3-FL-1 but RF-BF-2 has substantially lower metrics compared to RF-FL-1. This may indicate that a large proportion of the errors made by DL pipeline originates from the training of the fluorescence model U-Net3-FL-1 rather than the bright-field model U-Net3-BF-1. Interestingly, when comparing the U-Net3-FL-1 model predictions and the U-Net3-BF-1 model predictions directly to one another instead of comparing these to the manually generated ground truth, the corresponding F_1 score is 0.87. This is lower than the similarity between either the U-Net3-FL-1 model and manual ground truth (F_1 score = 0.91) or U-Net3-BF-1 and manual ground truth (F_1 score = 0.89). It means that the U-Net3-BF-1 model can surpass the prediction quality of the U-Net3-FL-1 model predictions in some instances while failing to do so in other cases. The ability of U-Net3-BF-1 to avoid at least some of the mispredictions generated by the U-Net3-FL-1 model could mean that the proposed strategy of bright-field model generation is likely to work even with relatively small manually annotated datasets without the risk of overfitting. Interestingly, the RF-FL-1 model has a higher F_1 score and MCC value compared to U-Net3-FL-1 model. However, these numbers should not be used to make conclusions about the general power of a particular machine-learning approach since the training sets for models were not identical. Different training sets were used for practical considerations. For example, the datasets were chosen to be small enough that would allow training of the models within a few hours and without the need for unconventionally large computational resources while still achieving sufficiently high quality.

Furthermore, analysing the competition, saturation and kinetic experiments, with both U-Net3-BF-1 and RF-BF-2 models provides the opportunity to compare the pipeline performances not only on the image level but also on the pharmacological level. As the most commonly used metric for fit quality, the R^2 values of the nonlinear model from each experiment were compared in a pairwise manner. The analysis revealed that the R^2 values obtained from the DL pipeline are statistically significantly higher compared to the RF pipeline ($p = 0.03$) calculated as described in 'Material and methods'. U-Net3-BF-1 based cell detection had a higher average R^2 values (mean = 0.93 ± 0.05 and median = 0.939) compared to the RF-BF-2 based cell detection pipeline (mean = 0.89 ± 0.09 and median = 0.911). The relatively large standard deviation of the R^2 values shows that the algorithmic uncertainty is not the primary source of uncertainty, and instead, the variability is caused by biological factors. The high average R^2 values indicate that both pipelines work well in general, and the difference is not very large in absolute terms, but also that the small inaccuracies in the cell segmentation stage are not cancelled out during the post-processing steps. Instead, the errors are carried over and degrade the final fitting quality. Therefore, the U-Net3 based DL pipeline can still offer considerable advantages over RF-based approach at both image level and downstream nonlinear regression level. Thus, from the quality perspective, it is reasonable to prefer the DL pipeline with U-Net3-BF-1 over the RF pipeline using the RF-BF-2 model. As the U-Net3-BF-1 model showed higher overall quality, all the following presented results were obtained using the DL pipeline.

## 3.6. Usability of deep learning and ilastik pipelines for microscopy image analysis

In addition to model quality, the usability aspects of the developed pipelines were compared. The most relevant ones were general computational hardware requirements, pipeline speed, the convenience of using the pipelines in terms of user interfaces, and finally, the convenience of developing new machine-learning models in case of adapting the developed assay for a different microscope or cell line.

It was identified that the speed of the ilastik based RF models is substantially slower compared to the U-Net3 based DL models used for analysing the microscopy images. The difference was especially evident in the case when a GPU (graphical processing unit) was used for computations, which considerably speeded up the DL models. A modern computer was able to analyse the results with both DL and ilastik pipelines in a comparable time for preparing an experiment or performing the imaging, thus, making the analysis quite manageable. On average, analysing a single 904 × 1224 pixel image took 12 s with RF pipeline and 3.5 s with DL pipeline.

Compared to spectroscopy methods, large data volumes generated by the microscopy experiments may cause storage issues. Therefore, before using the proposed microscopy methods, the user should make sure that sufficient memory is available for the experiments.

Another aspect to consider is the analysis convenience, which in the case of image analysis software is related to the need of manually adjusting the algorithm parameters and performing some of the image analysis, pre-processing, or post-processing steps manually. For both DL and ilastik pipelines, no manual parameter adjustment is needed removing one common obstacle in image analysis. In addition to choosing convenient machine-learning models, it was necessary to choose a suitable interface for using the machine-learning models and performing the pre and post-processing steps. Many such interfacing software tools such as FIJI (DeepImageJ [69]), CellProfiler [70] and ImJoy [71] allow almost unlimited flexibility for developing image analysis pipelines but also require that users have some knowledge of how image analysis pipelines work internally. These software currently also do not provide convenient out-of-the-box options for metadata handling required for pharmacological assays. Therefore, we chose Aparecium software (https://gpcr.ut.ee/aparecium.html) as the interfacing platform, as it is specifically designed for making image analysis pipelines as user-friendly as possible through graphical user interfaces (GUIs) while providing enough options for post-processing and metadata handling to carry out the biochemical analysis at the cost of less flexibility for general image analysis.

Finally, the aspect of machine-learning model development was considered as it is usually necessary to retrain the models from scratch or perform transfer learning if the method is used for widely different datasets [72,73]. In this study, two quite different model development environments were used. Model development in ilastik is relatively straightforward, requiring no programming skills and is done entirely through a GUI provided by the standalone ilastik software. Installing the software is very simple, and there are multiple tutorials available for using the GUI. Development of the DL models, including U-Net, is somewhat more difficult, requiring access to a python installation and preferentially to a
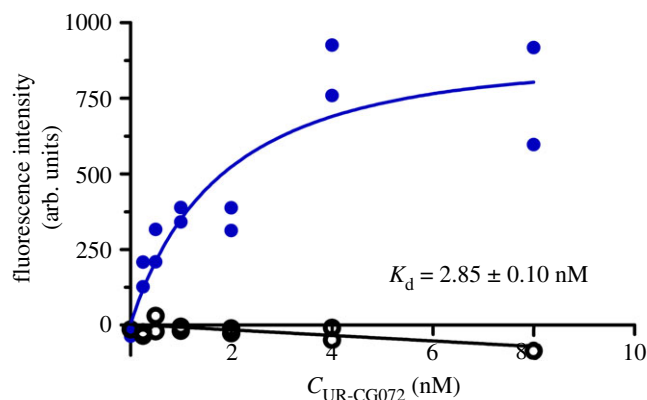
Figure 8. Saturation binding of UR-CG072 binding to live CHO-K1-hM$_4$R cells. The CHO-K1-hM$_4$R cells (25000 cells per well) were incubated for 5 h with two-fold serial dilutions of UR-CG072 in the range of 0–8 nM and with (non-specific binding, open black circle) or without (total binding, filled blue circle) 3.7 µM scopolamine. The background-corrected cells' fluorescence intensities were determined by the cell detection algorithm as described in 'Material and methods', and are presented as individual replicates from a representative experiment of three independent experiments performed in duplicate. Four images from different fields of view were taken from a single well.

Jupyter notebook server. However, this process is significantly simplified thanks to the recently developed ZeroCostDL4Mic framework [72]. ZeroCostDL4Mic reduces the training process to a point-and-click level without the need to adjust the code. Therefore, both ilastik and DL image analysis pipelines are sufficiently simplified that model training does not require extensive past experience with ilastik being the simplest option. Therefore, ilastik pipeline and the RF model is recommended for machine-learning applications where ease of use is more important than a slight loss in quality. These practical considerations are quite dynamic as software tools develop and are likely to change in the future.

3.7. Determination of binding affinities with UR-CG072 to M$_4$ receptor in live-cell microscopy

For determining the binding affinity of UR-CG072, an assay design similar to the radioligand saturation binding experiment was used. From these data a K_d of 2.85 ± 0.10 nM was obtained (figure 8), which is also in good agreement with all previous results (table 2). Interestingly, there is a small decline in non-specific binding with increasing concentration (figure 8), but it is not of biological origin and is instead explained by a shadow-imaging effect which is caused by non-specific binding of UR-CG072 to the well surface, making the background brighter than the cells. This effect, however, does not interfere with the overall measurement, and the slope is not statistically significantly different from 0. A control saturation binding experiment with CHO-K1 cells not expressing M$_4$ receptors shows that there is no ligand binding to the wild-type CHO-K1 cells (electronic supplementary material, figure S1) and thus all the observed binding is to the M$_4$ receptors.

Due to the good photostability of the 5-TAMRA label and the moderate kinetic rates of UR-CG072 binding, the k_{on} and k_{off} of UR-CG072 could be measured with the described live-cell system. The binding of UR-CG072 (figure 9) is fully reversible by the addition of 10 µM scopolamine after 3 h of

association (indicated by the arrow). Moreover, the K_d (2.6 ± 0.7 nM) obtained from kinetic data is in good agreement with previous values from both saturation binding assays as well as FA assays (table 2).

Lastly, competition binding experiments were carried out to confirm that the developed microscopy method is also suitable for screening novel unlabelled ligands in the future. Displacement curves were obtained for six ligands with varying structures, affinities and efficacies (figure 10). Regression analysis was used to obtain the IC$_{50}$ values from these data, which in turn were used to calculate pK_i values of the unlabelled ligands (table 3).

4. Discussion

The M$_4$ receptor is connected to multiple diseases and is, therefore, an interesting target for drug development. In modern drug screening, the fluorescence-based methods have gained popularity, but the limited availability of fluorescent ligands for the M$_4$ receptor has significantly hindered studies of this receptor. Recently, a set of new dibenzodiazepinone-type fluorescent ligands with high affinity to the M$_4$ receptor was synthesized, of which UR-MK342 and UR-CG072 were labelled with TAMRA [16]. In previous studies, TAMRA label has been successfully used in FA assays, among other methods [90–92]. Therefore, these probes are promising candidates for developing new ligand-binding assays for the M$_4$ receptor. Experimental results from the FA assay show that both UR-MK342 and UR-CG072 bind to M$_4$ receptors with high affinity, and the K_d values are in good agreement with previous radioligand binding measurements. Although both ligands also have sufficiently high signals and Z' values to be compatible with HTS assay standards, UR-CG072 is preferred in screening assays due to its faster binding kinetics, which allows reduction of required incubation time and mitigates the effects of evaporation and potential sedimentation.

Since UR-CG072 and UR-MK342 have previously been studied in the M$_2$ receptor FA assay system [17], similarities and differences in both receptor systems present an opportunity to gain more insight into their binding mechanism. Interestingly, the FA value of the receptor–ligand complex remains the same regardless of which receptor subtype, M$_2$ or M$_4$, is measured. This similarity is evident for both fluorescent ligands. By contrast, the receptor–ligand complex FA value depends on the fluorescent ligand is used and is consistently lower for UR-CG072 compared to UR-MK342 in complexes with both M$_2$ and M$_4$ receptor subtypes. This may indicate that the binding poses and the rotational freedom of the fluorophore moiety are similar between the two subtypes.

There are also some differences in the binding properties of these probes between the FA assays of M$_2$ and M$_4$ receptors. Both ligands seem to show a somewhat higher affinity towards the M$_2$ receptor, but the differences are relatively small [17]. This is expected as orthosteric binding sites of M$_2$ and M$_4$ are structurally very similar [9]. However, there could be differences in the binding site accessibility since the association kinetics of both probes to the M$_2$ receptor are faster compared to the M$_4$ receptor. This is not surprising as ligand binding to muscarinic receptors is known to be a complex process even for somewhat smaller ligands. For example, N-methylscopolamine first binds to the allosteric site before binding to the orthosteric site of the M$_2$ and M$_3$
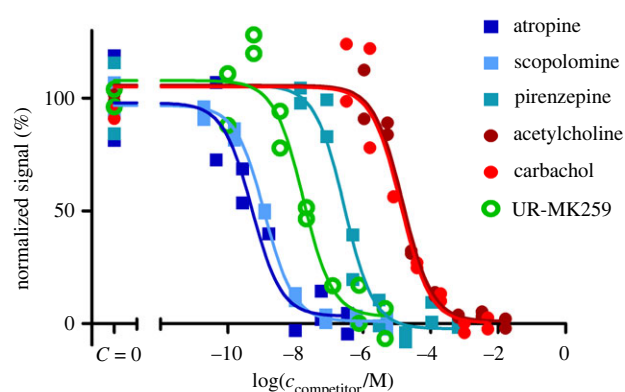
Table 2. Overview of binding parameters of UR-CG072 and UR-MK342.

	method	K_d (nM) ± s.e.m.	k_{on} (nM^{-1} min^{-1}) ± s.e.m.	k_{off} (min^{-1}) ± s.e.m.
UR-CG072	FA equilibrium	3.6 ± 1.1		
	FA kinetic SB toolbox	8.5 ± 0.8	0.0017 ± 0.0002	0.015 ± 0.002
	microscopy saturation	2.85 ± 0.10		
	microscopy kinetic	2.6 ± 0.7	0.017 ± 0.007	0.046 ± 0.004
	radioligand displacement (K_i)	3.7 ± 0.6 [16]		
UR-MK342	FA equilibrium	1.2 ± 0.5		
	FA kinetic SB toolbox	1.3 ± 0.4	0.0028 ± 0.0010	0.0037 ± 0.0012
	radioligand displacement (K_i)	0.97 ± 0.07 [16]		

k_{on}	0.0017 ± 0.007 min^{-1} nM^{-1}
k_{off}	0.046 ± 0.004 min^{-1}
$K_{d\_kinetic}$	2.6 ± 0.7 nM
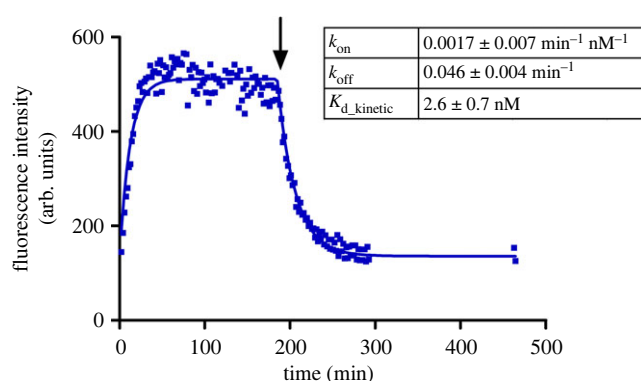
Figure 9. Association and dissociation of UR-CG072 (2 nM) to and from live CHO-K1-hM$_4$R cells. Dissociation was initiated with 5 µM scopolamine after 185 min (indicated with the arrow). A representative experiment of three independent experiments performed in duplicates is shown. Duplicate values are shown on the graph as separate points, to account for the measurement time difference between the replicates. Four images from different fields of view were taken from a single well. For analysis the GraphPad Prism model 'association then dissociation' was used.

Figure 10. Inhibition of UR-CG072 binding to live CHO-K1-hM$_4$R cells by muscarinic receptor ligands. The CHO-K1-hM$_4$R cells (25 000 cells per well) were incubated with 2 nM UR-CG072 and different concentrations of carbachol, arecoline, scopolamine, atropine, pirenzepine, and UNSW-MK259 for 120 min as described in 'Material and methods'. The cell fluorescence intensities were determined by the membrane detection algorithm using the U-Net3-BF-1 model and are presented as individual replicates from a representative experiment performed in duplicate. Four images from different fields of view were measured from a single well. Normalization was done separately for each ligand, 100% corresponds to wells where no competitors were added and 0% corresponds to the wells where the competitors' concentration is the largest.

receptor subtypes [93]. The most striking difference between ligand binding to M$_2$ and M$_4$ receptors is the apparent lack of a clear two-phase kinetic behaviour in the case of the M$_4$ receptor while it is present for the M$_2$ receptor. This could indicate that M$_2$ and M$_4$ receptor systems have differences beyond the orthosteric binding site properties as the two-phase behaviour of the M$_2$ receptor–ligand binding was not specific to FA or BBV system but was also present in nanoBRET assay with mammalian cells [17]. This may indicate heterogeneity of the M$_2$ receptor population, where receptors with multiple affinity states are present while the apparent heterogeneity is also ligand-dependent. For the M$_4$ receptor, such heterogeneity was not observed with the ligands used in this study. The nature of this heterogeneity remains elusive but may be explained by the simultaneous existence of M$_2$ receptor dimers and monomers or ligand interactions with M$_2$ receptor allosteric sites. Dimerization of the M$_2$ receptor is also supported by multiple previous studies while there is no information available about M$_4$ receptor dimerization [94–96].

The FA method with BBV particles has many advantages, such as kinetics measurement possibilities, relatively low cost, fast measurements and receptor source stability, which is achieved by using a single production batch of the BBV particle stock. Therefore, the FA-based assay is a suitable

option for HTS applications. However, there are also several differences between the BBV particle model system and *in vivo* or *ex vivo* conditions. For example, the live-cell systems allow studying G-protein and β-Arrestin signalling and other protein–protein interactions. Furthermore, cholesterol in the membrane has an effect on ligand binding to muscarinic receptors [97], thus using live mammalian cells allows obtaining more relevant measurement results. Therefore, a live cell-based assay system, although still having notable differences from *in vivo* systems, is a significant step closer to native systems. Live-cell assays also have some general disadvantages, such as slightly higher cost per experiment due to more advanced equipment required to perform the measurements and maintain cell culture. Additionally, live-cell measurements usually have higher uncertainty due to day-to-day variability. It must also be considered that the live-cell systems, which overexpress the receptors, do not fully reflect the natural system and may lead to considerable biases.

The results show that receptor–ligand complex formation on the surface of live cells can be studied by automated fluorescence

**Table 3.** Overview of unlabelled ligand affinities.

| unlabelled ligand | FA | | | | microscopy | | radioligand | |
| | UR-MK342 | | UR-CG072 | | UR-CG072 | | | |
	$pK_i \pm$ s.e.m.	N	$pK_i \pm$ s.e.m.	N	$pK_i \pm$ s.e.m.	N	$pK_i \pm$ s.e.m.	ref.
carbachol	3.7 ± 0.2	3	3.46 ± 0.09	3	5.28 ± 0.05	3	4.5 ± 0.3	[74–78]
arecoline	3.9 ± 0.2	3	3.52 ± 0.11	3	5.00 ± 0.03	3	5.0 ± 0.4	[74,77,79]
acetylcholine	4.5 ± 0.2	3	4.55 ± 0.09	3			4.60 ± 0.13	[77,80]
pilocarpine	4.7 ± 0.2	3	4.56 ± 0.09	3			5.31 ± 0.12	[74,77]
pirenzepine	6.3 ± 0.2	3	6.16 ± 0.08	3	6.95 ± 0.07	3	6.9 ± 0.2	[76–78,81–88]
scopolamine	8.30 ± 0.10	6	8.13 ± 0.09	3	9.18 ± 0.03	3	9.28 ± 0.19	[81,83]
atropine	8.62 ± 0.16	3	8.64 ± 0.09	3	10.33 ± 0.16	3	9.21 ± 0.10	[76–78,81,83–85,88,89]
UNSW-MK259	7.4 ± 0.2	3	8.64 ± 0.11	5	8.07 ± 0.03	3	8.6 ± 0.6	[63]
UR-SK75	9.0 ± 0.2	4	8.65 ± 0.08	3			8.6 ± 0.6	[50]
UR-SK59	8.9 ± 0.2	3	8.51 ± 0.08	3			8.6 ± 0.6	[50]

microscopy, which allows relatively fast measurements and high content spatio-temporal data collection. In addition, microscopy images can be used to study cell morphology, fluorophore localization, cell migration and cell death, which cannot be easily achieved with flow cytometry nor nanoBRET based measurement systems. These parameters can be useful for studying GPCR signalling [98]. Although a wide variety of advanced microscopy techniques allow measuring these parameters in great detail, high-end microscopy is often not automatic and, therefore, not suitable for high content studies. By contrast, automatic plate reader-based microscopes achieve a unique balance between the data volume and quality. This kind of automated live-cell microscopy has previously been used to study ligand binding to dopamine D_3 receptors [35]. In the present study, this method was further developed to enable the quantification of receptor–ligand binding in both equilibrium and kinetic modes. Faster kinetics of UR-CG072 compared to UR-MK342 favour using it in live-cell assays as shorter experiment times avoid negative effects such as cell detachment, changes in nutrient and oxygen concentration and cell death.

Although microscopy methods also pose some challenges related to data volumes, data analysis speed and data analysis pipeline usability, the results of this study show that suitable software and machine-learning models overcome these problems. The model comparison shows that while DL pipeline provides higher quality results, the ilastik pipeline models are easier to retrain. As the final pharmacological parameters obtained with U-Net3-BF-1 and RF-BF-2 models are similar, with an average $LogIC_{50}$ difference of 0.15 units between models from an individual displacement curve, then both options are viable in practice depending on the needed quality and user's level of expertise. A unique challenge with machine-learning-based image analysis pipelines is the need to retrain the models if a sufficiently large domain shift is introduced into the assay, such as changing the cell line or microscopy setup. Fortunately, this has to be done only once for a particular assay setup, and easy-to-use options exist for retraining the models. Altogether, the data analysis is not a limiting factor of the proposed live-cell assay.

Using the described live-cell microscopy approach combined with machine-learning-based data analysis allowed measuring ligand binding to M_4 receptor with high quality. It is important to mention that such quality can be achieved with the fluorescence signal of bound UR-CG072 being only 4% above the background, which is substantially less than almost 200% achieved with the human embryonic kidney 293 cells expressing dopamine D_3 receptors (HEK293-D_3R) system in a previous study [35]. This lower signal is caused by a combination of multiple factors. First, TAMRA fluorophore used in UR-CG072 has a lower quantum yield compared to Cy3B used in NAPS-Cy3B ligand. Second, the M_4 receptor is not expressed in all CHO-K1-hM_4R cells, while the D_3 receptor was expressed in HEK293 cells. As a final factor, using the cell culture medium instead of DPBS during imaging increases the image background intensity. Surprisingly, the reduction of the absolute signal by a factor of 50 does not affect the final uncertainty of the measurements to any significant extent. The obtained R^2 values for both saturation binding and displacement experiments are very similar for both D_3 and M_4 receptor microscopy assays. Essentially, it means that biological variability is the highest contributor to the total uncertainty while decreased signal has negligible uncertainty contribution. This, in turn, means that this kind of assay design should work just as well with either relatively low quantum yield fluorophores or vice-versa with systems that have receptor expression more comparable to physiological expression levels if a high brightness probe is available. Thus, the proposed approach to study ligand binding to receptors has a much wider application range than previously demonstrated. Finally, the current results prove the universality of this kind of microscopy assay, as switching to another receptor and cell line did not require major changes to the analysis pipeline or assay protocol.

The developed live-cell microscopy assay can be performed in the saturation binding mode, association and dissociation kinetic modes as well as in displacement experiments for measuring the affinity of unlabelled ligands. The kinetic measurements show that the fluorescence signal is quite stable once the equilibrium is reached after the association
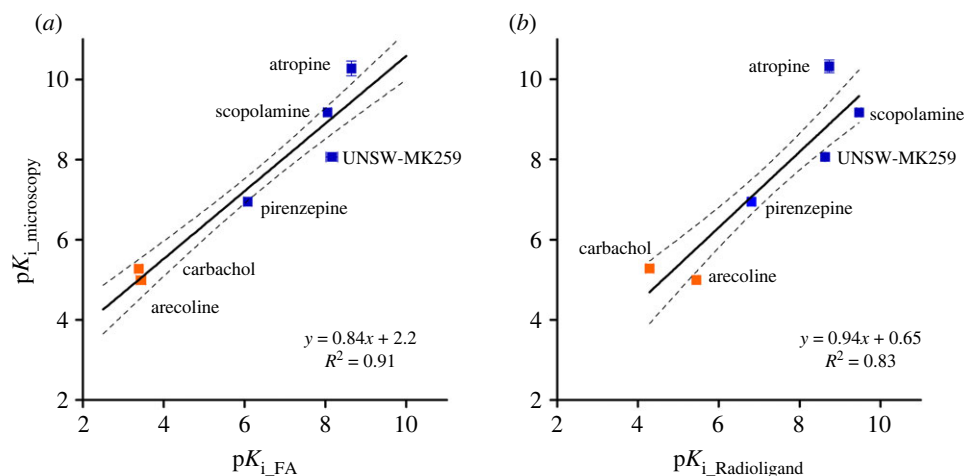
Figure 11. Correlation plots of affinities (pK_i values) of reported muscarinic receptor ligands measured with UR-CG072 in different assay systems. (a) Comparison of pK_i values determined in the microscopy competition binding assay and pK_i values obtained from the FA competition binding assay. (b) Comparison of pK_i values determined in the microscopy competition binding assay and pK_i values obtained from radioligand binding assay from literature (table 3). Investigated agonists are presented as orange symbols (filled orange square), antagonists as blue symbols (filled blue square). Black lines represent linear regression between the datasets and the dashed black line represent 95% confidence bands. Data shown for FA and microscopy is the mean of at least three independent experiments and the error bars represent s.e.m. Data shown for radioligand is the mean of values from articles shown in table 3 and the error bars represent s.e.m. of these data.

phase. It is also evident that scopolamine induces full displacement of UR-CG072 from the M_4 receptor as the signal reaches the same level as was in the starting point (figure 9). Although the signal does not reach zero after dissociation, this is caused by autofluorescence, not by incomplete dissociation. UR-CG072 also has sufficiently fast kinetics for performing association and dissociation kinetics so that the morphology of CHO-K1-hM$_4$R cells remains normal and the cells remain attached to the plate for the entire experiment. Both the kinetic measurements and saturation experiments prove that UR-CG072 retains its high affinity towards the M_4 receptor in the live-cell system, as expected from previous radioligand binding studies [16], while having a very low level of non-specific binding to the cells. This makes UR-CG072 a promising fluorescent probe also for more advanced microscopy methods such as live-cell total internal reflection fluorescence (TIRF) microscopy. The displacement curves obtained with UR-CG072 and unlabelled ligands have quite high quality and, therefore, this assay is suitable for the determination of affinities of unlabelled ligand binding to M_4 receptor. The system remains stable for the duration of long experiments meaning that accurate endpoint measurements can be obtained for an entire microplate even if imaging the full plate is not instantaneous. These properties also suggest that the assay can be used for small scale screening of novel ligands, for example, to confirm binding affinities in a live-cell system. The live-cell system is also internally consistent as the K_d values obtained from saturation binding measurements, and kinetic measurements are in excellent agreement.

Overall, the K_d values of UR-CG072 obtained from both saturation and kinetic FA and live-cell microscopy assays are in good agreement with each other (table 2 and figure 11). pK_i values of M_4 receptor ligands determined with the UR-CG072 using either FA or live-cell microscopy assay, were also in good agreement ($R^2 = 0.91$). The slope of the correlation was 0.84, while the intercept was 2.2. The live-cell method systematically estimates higher affinities for low-affinity ligands, while for high-affinity ligands in the nanomolar range, the estimated values are numerically more similar between the assays (figure 11). However, most low-affinity ligands are agonists, while high-affinity ligands are antagonists. Therefore, it is

difficult to determine whether there is a systematic difference between assays for low-affinity ligands or simply agonists. Agonism causing the systematic difference is theoretically well-founded, as the high-affinity receptor state is usually stabilized by G-proteins, which are not present in the BBV particles. A similarly good correlation was previously found between nanoBRET assay and FA assay using the same probe with M_2 receptor ($R^2 = 0.94$) with the same systematic differences between the pK_i values measured in BBV particles and live cells [17]. This further supports that the systematic difference between the determined agonist pK_i values is caused by differences between BBV particle and live-cell systems.

The developed live-cell microscopy assay can be modified for wider applications in the future. One development direction is further automatization of the assay by removing the remaining manual steps from the data analysis process. This could also include an even more standardized pipeline for machine-learning model development or a larger set of pre-trained models that cover the detection of the most common cell lines. We believe that it can be further developed to an extent to which the live-cell microscopy could also be used in an HTS context. Another development direction is a shift towards more natural systems such as tissue preparations, live tissues or tumour spheroids and measuring additional downstream signalling events in addition to ligand binding. Using these more challenging systems requires finding suitable fluorophores to overcome tissue autofluorescence and ligands with suitable kinetic properties to slow down fluorescence ligand dissociation during washing steps. Additionally, more advanced DL models may be necessary. The present study serves as a solid foundation for such developments.

As for the more general unlabelled ligand screening, both FA and live-cell microscopy methods and fluorescence ligands could be used as rapid and convenient options for guiding the synthesis of novel M_4 receptor ligands and allosteric modulators. Both methods also allow for kinetic measurements, which may help uncover more detailed binding mechanisms. Overall, choosing the suitable method for a specific experiment highly depends on the required throughput and availability of equipment. While FA

method with BBV particles fulfils many requirements of HTS applications, live cells are a vastly more flexible option for studying complex signalling pathways. Therefore, live-cell microscopy-based ligand-binding assays are likely to have an ever-growing role in future of ligand-binding studies.

References

1. Jeon J et al. 2010 A subpopulation of neuronal M_4 muscarinic acetylcholine receptors plays a critical role in modulating dopamine-dependent behaviors. J. Neurosci. 30, 2396–2405. (doi:10.1523/jneurosci.3843-09.2010)

2. Brodde O-E, Bruck H, Leineweber K, Seyfarth T. 2001 Presence, distribution and physiological function of adrenergic and muscarinic receptor subtypes in the human heart. Basic Res. Cardiol. 96, 528–538. (doi:10.1007/s003950170003)

3. Moro C, Uchiyama J, Chess-Williams R. 2011 Urothelial/lamina propria spontaneous activity and the role of M3 muscarinic receptors in mediating rate responses to stretch and carbachol. Urology 78, 1442. (doi:10.1016/j.urology.2011.08.039)

4. Haga T. 2013 Molecular properties of muscarinic acetylcholine receptors. Proc. Jpn. Acad. Ser. B Phys. Biol. Sci. 89, 226–256. (doi:10.2183/pjab.89.226)

5. Chan WY et al. 2008 Allosteric modulation of the muscarinic M_4 receptor as an approach to treating schizophrenia. Proc. Natl Acad. Sci. USA 105, 10 978–10 983. (doi:10.1073/pnas.0800567105)

6. Felder CC, Goldsmith PJ, Jackson K, Sanger HE, Evans DA, Mogg AJ, Broad LM. 2018 Current status of muscarinic M1 and M4 receptors as drug targets for neurodegenerative diseases. Neuropharmacology 136, 449–458. (doi:10.1016/j.neuropharm.2018.01.028)

7. Walker LC, Huckstep KL, Chen NA, Hand LJ, Lindsley CW, Langmead CJ, Lawrence AJ. 2021 Muscarinic M4 and M5 receptors in the ventral subiculum differentially modulate alcohol seeking versus consumption in male alcohol-preferring rats. Br. J. Pharmacol. 178, 3730–3746. (doi:10.1111/bph.15513)

8. Walker LC et al. 2020 Acetylcholine muscarinic M4 receptors as a therapeutic target for alcohol use disorder: converging evidence from humans and rodents. Biol. Psychiatry 88, 898–909. (doi:10.1016/j.biopsych.2020.02.019)

9. Thal DM et al. 2016 Crystal structures of the M1 and M4 muscarinic acetylcholine receptors. Nature 531, 335–340. (doi:10.1038/nature17188)

10. Jakubik J, El-Fakahany EE. 2020 Current advances in allosteric modulation of muscarinic receptors. Biomolecules 10, 325. (doi:10.3390/biom10020325)

11. Hoffmann C, Castro M, Rinken A, Leurs R, Hill SJ, Vischer HF. 2015 Ligand residence time at G-protein-coupled receptors-why we should take our time to study it. Mol. Pharmacol. 88, 552–560. (doi:10.1124/mol.115.099671)

12. Tahtaoui C, Parrot I, Klotz P, Guillier F, Galzi JL, Hibert M, Ilien B. 2004 Fluorescent pirenzepine derivatives as potential bitopic ligands of the human M1 muscarinic receptor. J. Med. Chem. 47, 4300–4315. (doi:10.1021/jm040800a)

13. Huwiler KG, De Rosier T, Hanson B, Vogel KW. 2010 A fluorescence anisotropy assay for the muscarinic M1 G-protein-coupled receptor. ASSAY Drug Devel. Technol. 8, 351–361. (doi:10.1089/adt.2009.0257)

14. Daval SB, Kellenberger E, Bonnet D, Utard V, Galzi JL, Ilien B. 2013 Exploration of the orthosteric/allosteric interface in human M1 muscarinic receptors by bitopic fluorescent ligands. Mol. Pharmacol. 84, 71–85. (doi:10.1124/mol.113.085670)

15. She X et al. 2020 Red-emitting dibenzodiazepinone derivatives as fluorescent dualsteric probes for the muscarinic acetylcholine M2 receptor. J. Med. Chem. 63, 4133–4154. (doi:10.1021/acs.jmedchem.9b02172)

16. Gruber CG, Pegoli A, Müller C, Grätz L, She X, Keller M. 2020 Differently fluorescence-labelled dibenzodiazepinone-type muscarinic acetylcholine receptor ligands with high M2R affinity. RSC Med. Chem. 11, 823–832. (doi:10.1039/D0MD00137F)

17. Grätz L, Laasfeld T, Allikalt A, Gruber CG, Pegoli A, Tahk M.-J., Tsernant M.-L., Keller M, Rinken A. 2021 BRET- and fluorescence anisotropy-based assays for real-time monitoring of ligand binding to M_2 muscarinic acetylcholine receptors. Biochim. Biophys. Acta Mol. Cell Res. 1868, 118930. (doi:10.1016/j.bbamcr.2020.118930)

18. Shivnaraine RV et al. 2016 Single-molecule analysis of the supramolecular organization of the M_2 muscarinic receptor and the Gαi1 protein. J. Am. Chem. Soc. 138, 11 583–11 598. (doi:10.1021/jacs.6b04032)

19. Nenasheva TA, Neary M, Mashanov GI, Birdsall NJM, Breckenridge RA, Molloy JE. 2013 Abundance, distribution, mobility and oligomeric state of M_2 muscarinic acetylcholine receptors in live cardiac muscle. J. Mol. Cell. Cardiol. 57, 129–136. (doi:10.1016/j.yjmcc.2013.01.009)

20. Hern JA, Baig AH, Mashanov GI, Birdsall B, Corrie JE, Lazareno S, Molloy JE, Birdsall NJ. 2010 Formation and dissociation of M1 muscarinic receptor dimers seen by total internal reflection fluorescence imaging of single molecules. Proc. Natl Acad. Sci. USA 107, 2693–2698. (doi:10.1073/pnas.0907915107)

21. Allikalt A, Kopanchuk S, Rinken A. 2018 Implementation of fluorescence anisotropy-based assay for the characterization of ligand binding to dopamine D1 receptors. Eur. J. Pharmacol. 839, 40–46. (doi:10.1016/j.ejphar.2018.09.008)

22. Hall MD, Yasgar A, Peryea T, Braisted JC, Jadhav A, Simeonov A, Coussens NP. 2016 Fluorescence polarization assays in high-throughput screening and drug discovery: a review. Methods Appl. Fluoresc. 4, 022001. (doi:10.1088/2050-6120/4/2/022001)

23. Link R, Veiksina S, Rinken A, Kopanchuk S. 2017 Characterization of ligand binding to melanocortin 4

receptors using fluorescent peptides with improved kinetic properties. *Eur. J. Pharmacol.* **799**, 58–66. (doi:10.1016/j.ejphar.2017.01.040)

24. Uri A, Nonga OE. 2020 What is the current value of fluorescence polarization assays in small molecule screening? *Expert Opin. Drug Discov.* **15**, 131–133. (doi:10.1080/17460441.2020.1702966)

25. Veiksina S, Tahk M-J, Laasfeld T, Link R, Kopanchuk S, Rinken A. 2021 Fluorescence anisotropy-based assay for characterization of ligand binding dynamics to GPCRs: the case of Cy3B-labeled ligands binding to MC4 receptors in budded baculoviruses. In *G protein-coupled receptor screening assays: methods and protocols* (eds SAM Martins, DMF Prazeres), pp. 119–136. New York, NY: Springer.

26. Rinken A, Lavogina D, Kopanchuk S. 2018 Assays with detection of fluorescence anisotropy: challenges and possibilities for characterizing ligand binding to GPCRs. *Trends Pharmacol. Sci.* **39**, 187–199. (doi:10.1016/j.tips.2017.10.004)

27. Veiksina S, Kopanchuk S, Rinken A. 2014 Budded baculoviruses as a tool for a homogeneous fluorescence anisotropy-based assay of ligand binding to G protein-coupled receptors: the case of melanocortin 4 receptors. *Biochim. Biophys. Acta Biomembr.* **1838**, 372–381. (doi:10.1016/j.bbamem.2013.09.015)

28. Wang Q, Bosch BJ, Vlak JM, van Oers MM, Rottier PJ, van Lent JWM.2016 Budded baculovirus particle structure revisited. *J. Invertebr. Pathol.* **134**, 15–22. (doi:10.1016/j.jip.2015.12.001)

29. Stoddart LA, White CW, Nguyen K, Hill SJ, Pfleger KDG. 2016 Fluorescence- and bioluminescence-based approaches to study GPCR ligand binding. *Br. J. Pharmacol.* **173**, 3028–3037. (doi:10.1111/bph.13316)

30. Pfleger KDG, Seeber RM, Eidne KA. 2006 Bioluminescence resonance energy transfer (BRET) for the real-time detection of protein-protein interactions. *Nat. Protoc.* **1**, 337–345. (doi:10.1038/nprot.2006.52)

31. Adan A, Alizada G, Kiraz Y, Baran Y, Nalbant A. 2017 Flow cytometry: basic principles and applications. *Crit. Rev. Biotechnol.* **37**, 163–176. (doi:10.3109/07388551.2015.1128876)

32. Esner M, Meyenhofer F, Bickle M. 2018 Live-cell high content screening in drug development. In *High content screening: a powerful approach to systems cell biology and phenotypic drug discovery* (eds PA Johnston, OJ Trask), pp. 149–164. New York, NY: Berlin, Germany: Springer.

33. Stoddart LA, Vernall AJ, Denman JL, Briddon SJ, Kellam B, Hill SJ. 2012 Fragment screening at adenosine-A(3) receptors in living cells using a fluorescence-based binding assay. *Chem. Biol.* **19**, 1105–1115. (doi:10.1016/j.chembiol.2012.07.014)

34. Lee PH, Miller SC, van Staden C, Cromwell EF. 2008 Development of a homogeneous high-throughput live-cell G-protein-coupled receptor binding assay. *J. Biomol. Screen.* **13**, 748–754. (doi:10.1177/1087057108317835)

35. Allikalt A, Laasfeld T, Ilisson M, Kopanchuk S, Rinken A. 2021 Quantitative analysis of fluorescent

ligand binding to dopamine D3 receptors using live-cell microscopy. *FEBS J.* **288**, 1514–1532. (doi:10.1111/febs.15519)

36. Place TL, Domann FE, Case AJ. 2017 Limitations of oxygen delivery to cells in culture: a underappreciated problem in basic and translational research. *Free Radic. Biol. Med.* **113**, 311–322. (doi:10.1016/j.freeradbiomed.2017.10.003)

37. Mou L, Gates A, Mosser VA, Tobin A, Jackson DA. 2006 Transient hypoxia induces sequestration of M_1 and M_2 muscarinic acetylcholine receptors. *J. Neurochem.* **96**, 510–519. (doi:10.1111/j.1471-4159.2005.03571.x)

38. Lin T-Y, Maire M, Belongie S, Hays J, Perona P, Ramanan D, Dollár P, Zitnick CL. 2014 Year microsoft COCO: common objects in context. In *Computer vision – ECCV 2014* (eds D Fleet, T Pajdla, B Schiele, T Tuytelaars), pp. 740–755. Cham, Switzerland: Springer International Publishing.

39. Cordts M, Omran M, Ramos S, Rehfeld T, Enzweiler M, Benenson R, Franke U, Roth S, Schiele B. 2016 The cityscapes dataset for semantic urban scene understanding. In *Computer Vision and Pattern Recognition* (CVPR), *Las Vegas, NV, USA, 27–30 June 2016, pp.* 3213–3223. Piscataway, NJ: IEEE Xplore. (doi:10.1109/CVPR.2016.350)

40. Caicedo JC *et al.* 2019 Evaluation of deep learning strategies for nucleus segmentation in fluorescence images. *Cytometry A* **95**, 952–965. (doi:10.1002/cyto.a.23863)

41. He K, Gkioxari G, Dollár P, Girshick R. 2017 Mask R-CNN. *IEEE Int. Conf. on Computer Vision (ICCV), Venice, Italy, 22–29 October 2017*, pp. 2980–2988. Piscataway, NJ: IEEE Computer Society. (doi:10.1109/ICCV.2017.322)

42. Bannon D *et al.* 2021 DeepCell Kiosk: scaling deep learning–enabled cellular image analysis with Kubernetes. *Nat. Methods* **18**, 43–45. (doi:10.1038/s41592-020-01023-0)

43. Falk T *et al.* 2019 U-Net: deep learning for cell counting, detection, and morphometry. *Nat. Methods* **16**, 67–70. (doi:10.1038/s41592-018-0261-2)

44. Badrinarayanan V, Kendall A, Cipolla R. 2017 SegNet: a deep convolutional encoder-decoder architecture for image segmentation. *IEEE Trans. Pattern Anal. Mach. Intell.* **39**, 2481–2495. (doi:10.1109/TPAMI.2016.2644615)

45. Minaee S, Boykov Y, Porikli F, Plaza A, Kehtarnavaz N, Terzopoulos D. In press. Image segmentation using deep learning: a survey. *IEEE Trans. Pattern Anal. Mach. Intell.* (doi:10.1109/TPAMI.2021.3059968)

46. Kraus OZ, Grys BT, Ba J, Chong Y, Frey BJ, Boone C, Andrews BJ. 2017 Automated analysis of high-content microscopy data with deep learning. *Mol. Syst. Biol.* **13**, 924. (doi:10.15252/msb.20177551)

47. Ronneberger O, Fischer P, Brox T. 2015 Year U-Net: convolutional networks for biomedical image segmentation. In *Medical image computing and computer-assisted intervention – MICCAI 2015* (eds N Navab, J Hornegger, WM Wells, AF Frangi), pp. 234–241. Cham, Switzerland: Springer International Publishing.

48. Redmon J, Divvala S, Girshick R, Farhadi A. 2016 You only look once: unified, real-time object

detection. In *Proceedings of the IEEE Conference on Computer Vision and Pattern Recognition (CVPR), Las Vegas, USA, 26 June–1 July 2016*, pp. 779–788. Piscataway, NJ: IEEE Computer Society. (doi:10.1109/CVPR.2016.91)

49. Fishman D, Salumaa S-O, Majoral D, Laasfeld T, Peel S, Wildenhain J, Schreiner A, Palo K, Parts L. 2021 Practical segmentation of nuclei in brightfield cell images with neural networks trained on fluorescently labelled samples. *J. Microsc.* **284**, 12–24. (doi:10.1111/jmi.13038)

50. She X, Pegoli A, Mayr J, Hübner H, Bernhardt G, Gmeiner P, Keller M. 2017 Heterodimerization of dibenzodiazepinone-type muscarinic acetylcholine receptor ligands leads to increased M2R affinity and selectivity. *ACS Omega* **2**, 6741–6754. (doi:10.1021/acsomega.7b01085)

51. Keller M, Tränkle C, She X, Pegoli A, Bernhardt G, Buschauer A, Read RW. 2015 M2 subtype preferring dibenzodiazepinone-type muscarinic receptor ligands: effect of chemical homo-dimerization on orthosteric (and allosteric?) binding. *Bioorg. Med. Chem.* **23**, 3970–3990. (doi:10.1016/j.bmc.2015.01.015)

52. Laasfeld T, Kopanchuk S, Rinken A. 2017 Image-based cell-size estimation for baculovirus quantification. *Biotechniques* **63**, 161–168. (doi:10.2144/000114595)

53. Berg S *et al.* 2019 ilastik: interactive machine learning for (bio)image analysis. *Nat. Methods.* **16**, 1226–1232. (doi:10.1038/s41592-019-0582-9)

54. Jung AB. 2021 Imgaug. See https://github.com/aleju/imgaug (accessed 30 December 2021).

55. Kingma DP, Ba J. 2014 Adam: a method for stochastic optimization. *arXiv*, 1412.6980. (doi: 10.48550/arXiv.1412.6980)

56. Ali MAS, Misko O, Salumaa S-O, Papkov M, Palo K, Fishman D, Parts L. 2021 Evaluating very deep convolutional neural networks for nucleus segmentation from brightfield cell microscopy images. *SLAS Discov.* **26**, 1125–1137. (doi:10.1177/24725552211023214)

57. Chollet F. Keras. See https://github.com/keras-team/keras (accessed 30.12.2021).

58. Tartu U. o. UT Rocket. See https://share.neic.no/#/marketplace-public-offering/c8107e145e0d41f7a016b72825072287/.

59. Lakowicz JR. 2006 *Principles of fluorescence spectroscopy*, 954p. Berlin, Germany: Springer.

60. Cheng Y-C, Prusoff WH. 1973 Relationship between the inhibition constant (KI) and the concentration of inhibitor which causes 50 per cent inhibition (I50) of an enzymatic reaction. *Biochem. Pharmacol.* **22**, 3099–3108. (doi:10.1016/0006-2952(73)90196-2)

61. Zhang JH, Chung TD, Oldenburg KR. 1999 A simple statistical parameter for use in evaluation and validation of high throughput screening assays. *J. Biomol. Screen.* **4**, 67–73. (doi:10.1177/108705719900400206)

62. Allikalt A, Rinken A. 2017 Budded baculovirus particles as a source of membrane proteins for radioligand binding assay: the case of dopamine D1 receptor. *J. Pharmacol. Toxicol. Methods* **86**, 81–86. (doi:10.1016/j.vascn.2017.04.004)

63. Pegoli A, She X, Wifling D, Hübner H, Bernhardt G, Gmeiner P, Keller M. 2017 Radiolabeled dibenzodiazepinone-type antagonists give evidence of dualsteric binding at the M2 muscarinic acetylcholine receptor. *J. Med. Chem.* **60**, 3314–3334. (doi:10.1021/acs.jmedchem.6b01892)

64. Kluyver T *et al.* 2016 Jupyter notebooks: a publishing format for reproducible computational workflows. In *Positioning and power in academic publishing: players, agents and agendas*, pp. 87–90. Amsterdam, The Netherlands: IOS Press.

65. 2D+Time Datasets - Cell Tracking Challenge. See http://celltrackingchallenge.net/2d-datasets/.

66. Maška M *et al.* 2014 A benchmark for comparison of cell tracking algorithms. *Bioinformatics* **30**, 1609–1617. (doi:10.1093/bioinformatics/btu080)

67. Scherr T, Löffler K, Böhland M, Mikut R. 2020 Cell segmentation and tracking using CNN-based distance predictions and a graph-based matching strategy. *PLoS ONE* **15**, e0243219. (doi:10.1371/journal.pone.0243219)

68. Scherr T, Löffler K, Neumann O, Mikut R. 2021 On Improving an Already Competitive Segmentation Algorithm for the Cell Tracking Challenge - Lessons Learned. *bioRxiv.* 2021.2006.2026.450019. (doi:10.1101/2021.06.26.450019)

69. Gómez-de-Mariscal E, García-López-de-Haro C, Ouyang W, Donati L, Lundberg E, Unser M, Muñoz-Barrutia A, Sage D. 2021 DeepImageJ: a user-friendly environment to run deep learning models in ImageJ. *Nat. Methods* **18**, 1192–1195. (doi:10.1038/s41592-021-01262-9)

70. McQuin C *et al.* 2018 CellProfiler 3.0: next-generation image processing for biology. *PLoS Biol.* **16**, e2005970. (doi:10.1371/journal.pbio.2005970)

71. Ouyang W, Mueller F, Hjelmare M, Lundberg E, Zimmer C. 2019 ImJoy: an open-source computational platform for the deep learning era. *Nat. Methods* **16**, 1199–1200. (doi:10.1038/s41592-019-0627-0)

72. von Chamier L *et al.* 2021 Democratising deep learning for microscopy with ZeroCostDL4Mic. *Nat. Commun.* **12**, 2276. (doi:10.1038/s41467-021-22518-0)

73. Shin HC, Roth HR, Gao M, Lu L, Xu Z, Nogues I, Yao J, Mollura D, Summers RM. 2016 Deep convolutional neural networks for computer-aided detection: CNN architectures, dataset characteristics and transfer learning. *IEEE Trans. Med. Imaging* **35**, 1285–1298. (doi:10.1109/TMI.2016.2528162)

74. Jakubík J, Bačáková, L., El-Fakahany EE, Tuček S. 1997 Positive cooperativity of acetylcholine and other agonists with allosteric ligands on muscarinic acetylcholine receptors. *Mol. Pharmacol.* **52**, 172–179. (doi:10.1124/mol.52.1.172)

75. Wood MD, Murkitt KL, Ho M, Watson JM, Brown F, Hunter AJ, Middlemiss DN. 1999 Functional comparison of muscarinic partial agonists at muscarinic receptor subtypes hM_1, hM_2, hM_3, hM_4 and hM_5 using microphysiometry. *Br. J. Pharmacol.* **126**, 1620–1624. (doi:10.1038/sj.bjp.0702463)

76. Kashihara K, Varga EV, Waite SL, Roeske WR, Yamamura HI. 1992 Cloning of the rat m_3, m_4 and m_5 muscarinic acetylcholine receptor genes by the polymerase chain reaction (PCR) and the pharmacological characterization of the expressed genes. *Life Sci.* **51**, 955–971. (doi:10.1016/0024-3205(92)90403-C)

77. Dong GZ, Kameyama K, Rinken A, Haga T. 1995 Ligand binding properties of muscarinic acetylcholine receptor subtypes (m1-m5) expressed in baculovirus-infected insect cells. *J. Pharmacol. Exp. Ther.* **274**, 378–384. (doi:10.1016/s0021-5198(19)50375-4)

78. Rinken A, Kameyama K, Haga T, Engström L. 1994 Solubilization of muscarinic receptor subtypes from baculovirus infected sf9 insect cells. *Biochem. Pharmacol.* **48**, 1245–1251. (doi:10.1016/0006-2952(94)90162-7)

79. Ozenil M *et al.* 2020 Enhanced arecoline derivatives as muscarinic acetylcholine receptor M1 ligands for potential application as PET radiotracers. *Eur. J. Med. Chem.* **204**, 112623. (doi:10.1016/j.ejmech.2020.112623)

80. Keov P, Valant C, Devine SM, Lane JR, Scammells PJ, Sexton PM, Christopoulos A. 2013 Reverse engineering of the selective agonist TBPB unveils both orthosteric and allosteric modes of action at the M_1 muscarinic acetylcholine receptor. *Mol. Pharmacol.* **84**, 425. (doi:10.1124/mol.113.087320)

81. Bolden C, Cusack B, Richelson E. 1992 Antagonism by antimuscarinic and neuroleptic compounds at the five cloned human muscarinic cholinergic receptors expressed in Chinese hamster ovary cells. *J. Pharmacol. Exp. Ther.* **260**, 576–580.

82. Dörje F, Wess J, Lambrecht G, Tacke R, Mutschler E, Brann MR. 1991 Antagonist binding profiles of five cloned human muscarinic receptor subtypes. *J. Pharmacol. Exp. Ther.* **256**, 727–733. (doi:10.1111/j.1476-5381.1991.tb12161.x)

83. Huang F, Buchwald P, Browne CE, Farag HH, Wu W-M, Ji F, Hochhaus G, Bodor N. 2001 Receptor binding studies of soft anticholinergic agents. *AAPS PharmSci.* **3**, 44–56. (doi:10.1208/ps030430)

84. Hegde SS, Choppin A, Bonhaus D, Briaud S, Loeb M, Moy TM, Loury D, Eglen RM. 1997 Functional role of M_2 and M_3 muscarinic receptors in the urinary bladder of rats *in vitro* and *in vivo*. *Br. J. Pharmacol.* **120**, 1409–1418. (doi:10.1038/sj.bjp.0701048)

85. Croy CH, Chan WY, Castetter AM, Watt ML, Quets AT, Felder CC. 2016 Characterization of PCS1055, a novel muscarinic M4 receptor antagonist. *Eur. J. Pharmacol.* **782**, 70–76. (doi:10.1016/j.ejphar.2016.04.022)

86. Jolkkonen M, van Giersbergen PLM, Hellman U, Wernstedt C, Karlsson E. 1994 A toxin from the green mamba *Dendroaspis angusticeps*: amino acid sequence and selectivity for muscarinic m4 receptors. *FEBS Lett.* **352**, 91–94. (doi:10.1016/0014-5793(94)00933-3)

87. Wess J, Lambrecht G, Mutschler E, Brann MR, Dörje F. 1991 Selectivity profile of the novel muscarinic antagonist UH-AH 37 determined by the use of cloned receptors and isolated tissue preparations. *Br. J. Pharmacol.* **102**, 246–250. (doi:10.1111/j.1476-5381.1991.tb12161.x)

88. Peralta EG, Ashkenazi A, Winslow JW, Smith DH, Ramachandran J, Capon DJ. 1987 Distinct primary structures, ligand-binding properties and tissue-specific expression of four human muscarinic acetylcholine receptors. *EMBO J.* **6**, 3923–3929. (doi:10.1002/j.1460-2075.1987.tb02733.x)

89. Hirose H *et al.* 2001 Pharmacological Properties of (2R)-N-[1-(6-Aminopyridin-2-ylmethyl)piperidin-4-yl]-2-[(1R)-3,3-difluorocyclopentyl]-2- hydroxy-2-phenylacetamide: a novel muscarinic antagonist with M2-sparing antagonistic activity. *J. Pharmacol. Exp. Ther.* **297**, 790–797. (doi:10.1002/chin.200113139)

90. Veiksina S, Kopanchuk S, Rinken A. 2010 Fluorescence anisotropy assay for pharmacological characterization of ligand binding dynamics to melanocortin 4 receptors. *Anal. Biochem.* **402**, 32–39. (doi:10.1016/j.ab.2010.03.022)

91. Harley MJ, Toptygin D, Troxler T, Schildbach JF. 2002 R150A mutant of F Tral relaxase domain: reduced affinity and specificity for single-stranded DNA and altered fluorescence anisotropy of a bound labeled oligonucleotide. *Biochemistry* **41**, 6460–6468. (doi:10.1021/bi011969i)

92. Stoddart LA, Johnstone EKM, Wheal AJ, Goulding J, Robers MB, Machleidt T, Wood KV, Hill SJ, Pfleger KDG. 2015 Application of BRET to monitor ligand binding to GPCRs. *Nat. Methods* **12**, 661–663. (doi:10.1038/nmeth.3398)

93. Jakubík J, Randáková A, Zimčík P, El-Fakahany EE, Doležal V. 2017 Binding of N-methylscopolamine to the extracellular domain of muscarinic acetylcholine receptors. *Sci. Rep.* **7**, 40381. (doi:10.1038/srep40381)

94. Marsango S, Ward RJ, Alvarez-Curto E, Milligan G. 2018 Muscarinic receptor oligomerization. *Neuropharmacology* **136**, 401–410. (doi:10.1016/j.neuropharm.2017.11.023)

95. Park PSH, Wells JW. 2004 Oligomeric potential of the M2 muscarinic cholinergic receptor. *J. Neurochem.* **90**, 537–548. (doi:10.1111/j.1471-4159.2004.02536.x)

96. Pisterzi LF, Jansma DB, Georgiou J, Woodside MJ, Chou JT-C, Angers S, Raicu V, Wells JW. 2010 Oligomeric size of the M2 muscarinic receptor in live cells as determined by quantitative fluorescence resonance energy transfer. *J. Biol. Chem.* **285**, 16 723–16 738. (doi:10.1074/jbc.M109.069443)

97. Michal P, Rudajev V, El-Fakahany EE, Doležal V. 2009 Membrane cholesterol content influences binding properties of muscarinic M2 receptors and differentially impacts activation of second messenger pathways. *Eur. J. Pharmacol.* **606**, 50–60. (doi:10.1016/j.ejphar.2009.01.028)

98. Revankar CM, Vines CM, Cimino DF, Prossnitz ER. 2004 Arrestins block G protein-coupled receptor-mediated apoptosis. *J. Biol. Chem.* **279**, 24 578–24 584. (doi:10.1074/jbc.M402121200)

99. Tahk M-J *et al.* 2022 Live-cell microscopy or fluorescence anisotropy with budded baculoviruses—which way to go with measuring ligand binding to M_4 muscarinic receptors? Figshare. (doi:10.6084/m9.figshare.c.6002187)